POLITECNICO
MILANO 1863

DIPARTIMENTO DI MECCANICA

mecc

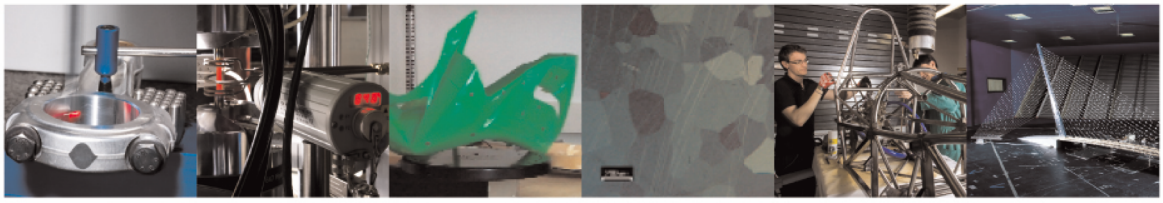

A novel 1D iFEM framework for structural health monitoring under degrading boundary conditions

Bardiani, Jacopo; Orsenigo, Francesco; Manes, Andrea; Sbarufatti, Claudio

This manuscript has been accepted for publication in Structural Health Monitoring. This is the author accepted manuscript (AAM), and it has not been copyedited or formatted for final publication.
Bardiani J, Orsenigo F, Manes A, Sbarufatti C. A novel 1D iFEM framework for structural health monitoring under degrading boundary conditions. Structural Health Monitoring. 2026;0(0). doi:10.1177/14759217251408513

A novel 1D Inverse FEM framework for Structural Health Monitoring under degrading boundary conditions

Authors: Jacopo Bardiani[a,*], Francesco Orsenigo[a], Andrea Manes[a] and Claudio Sbarufatti[a]

[a] *Politecnico di Milano, Department of Mechanical Engineering, Via G. La Masa 1, 20156 Milano, Italy*

***Corresponding Author:** Jacopo Bardiani, Department of Mechanical Engineering, Politecnico di Milano, Via G. La Masa 1; +39 02 2399 8500, jacopo.bardiani@polimi.it

Abstract

The inverse Finite Element Method (iFEM) reconstructs full-field displacements from strain data without prior knowledge of loads or material properties. However, unknown or time-varying boundary conditions can degrade shape-sensing accuracy. This work advances smart sensing and structural health monitoring for beam-like structures by coupling iFEM with an online identification of boundary-condition degradation. An aluminum beam instrumented with an FBG sensor network is tested under controlled degradations—rotational stiffness reduction and vertical support settlement—each modeled as a virtual spring with unknown stiffness. A nonlinear optimization routine estimates the spring parameters while iFEM performs real-time shape reconstruction. Results show high-accuracy displacement fields and reliable quantification of support degradation, with a maximum deviation of about 10% from ground truth for both rotational and vertical cases. The framework demonstrates practical feasibility for simultaneous shape sensing and boundary-condition assessment in operational environments.

Keywords: Degrading boundary conditions; shape sensing; inverse Finite Element Method; Fiber-Bragg-Gratings; virtual springs; Structural Health Monitoring

Highlights

- iFEM enables accurate shape sensing of structures with degrading boundary conditions.
- A novel procedure estimates boundary stiffness degradation using virtual springs and FBG strain data.
- Experimental validation under two common scenarios: rotation and vertical degradation.
- The framework supports real-time structural health monitoring and adaptive maintenance strategies for different types of beam-like structure.

1. Introduction

Failures in civil infrastructure arise from material deterioration and human/operational factors [1]. Bridges are emblematic because of their societal role and the severe consequences of collapse. Failures occur across materials (steel and concrete) [2]; the leading causes—design/construction errors, overloading, scour, and collision—account for over 70% of cases [1]. Durability is further reduced by concurrent physical and chemical mechanisms (freeze–thaw, salt crystallization, chloride-induced corrosion) that damage concrete and reinforcing steel [3–5].

Inspection and maintenance—typically within a ~75-year design life with biennial checks—are essential but constrained by access and cost; materials and protective systems can mitigate risks but are not sufficient alone [6–7]. Recent events (e.g., Morandi Bridge) illustrate how deferred maintenance and progressive degradation can precipitate collapse and retrospective analyses indicate such failures could be anticipated with better condition tracking [8–15].

Structural Health Monitoring (SHM) supports data-driven decisions via sensor networks, with deflection/shape an early indicator of distress [16–20]. Multiple SHM approaches have been developed, utilizing features such as strain, acoustic emissions, vibration signals, and electromechanical impedance, measured by diverse sensors and processed through statistical analysis [15,18–22]. Despite progress, these methods face practical challenges—sensor placement, debonding, and information dispersion—and often depend on fixed reference points that are difficult to maintain due to traffic, waterways, terrain, vandalism, or foundation movements [21–25]. This limitation has spurred reference-free strategies (also known as shape-sensing techniques) that infer deflections directly from strain [26–36]—most notably modal-based fitting [37–40], direct strain integration [41,42], and iFEM [43,44]—which avoid external reference points and support continuous, in-situ monitoring.

The iFEM strategy is particularly attractive due to its independence from external loads and material properties, and its ability to accommodate complex geometries and boundary conditions. Initially proposed by Tessler and Spangler for shell structures [43,45], iFEM was extended to Timoshenko beams [46, 47], slender Euler-Bernoulli beams [48], and curved beam elements [49]. Its applications span aerospace, mechanical, and energy sectors [50–54], as well as civil engineering, including tunnel monitoring [55] and bridge assessment [56]. Unlike optimization-heavy methods like Genetic Algorithms or Particle Swarm Optimization [57–63], iFEM is computationally efficient and suited for real-time use with distributed or discrete strain sensors such as Fiber Bragg Gratings (FBGs). More recently, the iFEM framework has also been extended by coupling it with Generalised Beam Theory (GBT) to enhance shape sensing and damage detection capabilities in thin-walled cylindrical and conical shell structures, further broadening its applicability to several pressure vessel configurations [64,65].

Despite its strengths, iFEM still requires accurate knowledge of boundary conditions, which are often uncertain or entirely unavailable—an issue that can lead to reconstruction failure and inaccurate results. This challenge is particularly evident in structures exposed to environmental effects that alter boundary conditions over time. For instance, scour and corrosion phenomena can alter support conditions of bridges over time, introducing settlements and rotations at foundations that invalidate original assumptions [66]. Similarly, wind turbines, offshore platforms, and subsea pipelines are vulnerable to shifting soil and seabed erosion, leading to variable support conditions. In particular, the foundations of wind turbines, both onshore and offshore, have been increasingly studied within

the SHM framework, as foundation degradation can lead to catastrophic failures given the limited redundancy typically present in their structural design [67–68].
However, the issue of uncertain boundary conditions is not confined to ground-based structures. It extends to a wide range of engineered systems, including steel frames where beam-to-column connections rely on mechanical fasteners [69,70], and even to aircraft structures, such as the attachment of wings to the fuselage. These connections are often idealized as perfectly rigid during the design phase; however, over time, their stiffness degrades due to factors such as fatigue, thermal expansion, and microcracking. Therefore, the challenge posed by degrading or uncertain boundary conditions must be tackled explicitly to ensure that iFEM remains a robust tool in real-world applications.

This issue has received limited attention in the current SHM literature. In fact, existing works mostly focus on boundary identification using modal analysis or natural frequencies [71–76], while other researchers employ static flexibility metrics, but still require load and material knowledge [76]. A notable exception is the work by Colombo et al. [77], who employed vision-based systems to evaluate linear combinations of configurations with differing boundary conditions on a composite plate, marking one of the first attempts at boundary condition estimation in an iFEM context. However, the applicability of this methodology to real cases is limited due to the practical challenges associated with camera placement.

To address this gap, the present work proposes a novel framework specifically designed to incorporate the effects of boundary condition degradation of hyperstatic structures into the iFEM formulation. To the best of the author's knowledge, this work is the first to systematically address boundary condition degradation conditions in iFEM-based monitoring exclusively using FBG sensors. Overall, the method's key innovations are twofold:

(1) Develop an effective methodology for real-time shape sensing of structures with degrading boundary conditions, overcoming the intrinsic limitation of iFEM which relies on complete and accurate knowledge of the boundary constraints.
(2) Develop a strategy to quantify the change in stiffness of degraded boundary conditions relative to the healthy state baseline, and to identify the updated stiffness value to be implemented in a direct FEM analysis for retrofitting purposes.

To achieve these two objectives, the proposed framework extends iFEM by introducing virtual springs at degraded boundary degrees of freedom and reconstructing the corresponding displacements from strain measurements using beam theory. These estimated displacements are then imposed via Lagrange multipliers, ensuring accurate shape sensing despite unknown or degraded constraints—thus addressing (1). To fulfill (2), a nonlinear optimization process is employed to identify the stiffness of the virtual springs. This allows quantifying boundary degradation without requiring material properties or external loads. The validation of the framework is based on an experimental aluminum beam with strain data from static tests. Two scenarios are examined under progressive degradation: a clamped–clamped beam where one clamp deteriorates to a pin with an unknown, decreasing rotational spring; and a clamped–simply supported beam where the simple support becomes a vertical spring with unknown, decreasing stiffness. These cases emulate typical boundary-stiffness decay observed in practical applications.

The paper is structured as follows. Section 2 presents the theory of the iFEM formulation and its coupling with degrading boundary conditions. Section 3 highlights the framework's steps which have been developed to extract the degradation parameters from the iFEM analysis. Section 4 outlines the experimental studies, detailing the experimental setup, the sensor network and their integration into the iFEM framework. Section 5 discusses the results obtained, including the reconstruction of full-

field displacement and strain for the scenarios investigated. Section 6 concludes the paper, summarizing key findings and their implications for future research and applications.

2. 1D inverse Finite Element Method review with degrading boundary conditions

A brief review of the 1D iFEM approach for displacement and strain field reconstruction is provided in this section, also accounting for the presence of degrading boundary conditions. The discussion is divided into subsections to better expose the required procedure's steps. Section 2.1 introduces the classical 1D iFEM methodology, Section 2.2 describes the standard formulation for applying boundary conditions in the iFEM framework, Section 2.3 presents the hybrid direct-Lagrange method for equivalent stiffness estimation; and Section 2.4 addresses the evaluation of boundary condition degradation.

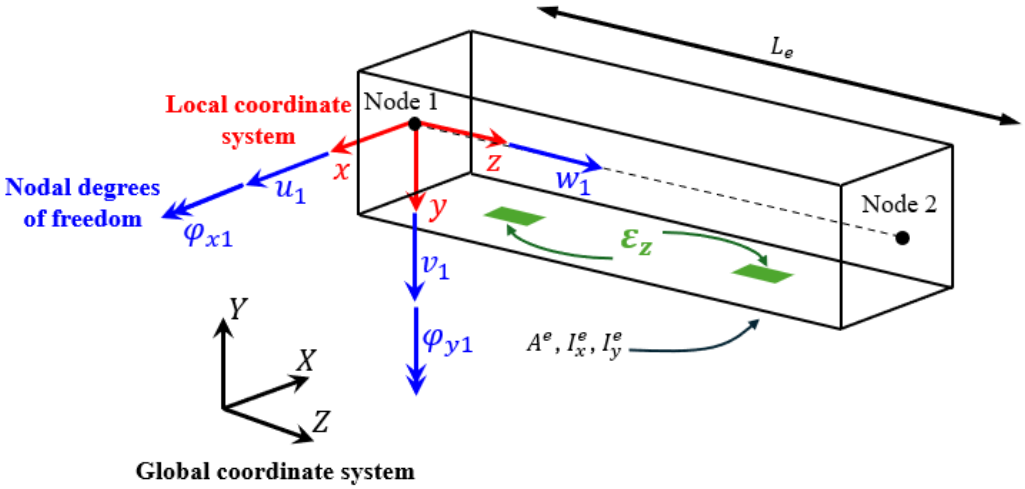

Figure 1 Geometrical properties and kinematic parameters of the 1D beam inverse element.

2.1 1D iFEM methodology

Consider a straight beam with constant cross-section, in the Cartesian reference system (x, y, z), as shown in Figure 1. The reference system has the z axis coinciding with the longitudinal axis of the beam and the x and y axes are the section's principal axes of inertia. The element of length L and section area A is characterized by the moments of inertia I_x and I_y referred, respectively, to the x and y axes. The constituent material is elastic, homogeneous and isotropic with the following mechanical properties: E (Young's modulus), G (shear modulus) and υ (Poisson coefficient). If torsion does not occur, the kinematics of the beam in space is defined by the following displacement field:

$$\begin{cases} u_x(x,y,z) = u(z) \\ u_y(x,y,z) = v(z) \\ u_z(x,y,z) = w(z) + y \cdot \varphi_x(z) - x \cdot \varphi_y(z) \end{cases} \tag{1}$$

Where u_x, u_y, u_z are the displacements in the x, y and z directions; w, v and u are the displacements of the section's centroid at the axial position z; φ_x and φ_y are the rotations around the x and y axis, respectively, as visible in Figure 1. These kinematic variables are grouped into the vector $\boldsymbol{u} = [w, v, \varphi_x, u, \varphi_y]^T$. Assuming linearity and according to the Euler-Bernoulli kinematic theory, the only non-null strain component is strain in z direction, ε_z, can be expressed as follow:

$$\varepsilon_z(x,y,z) = \varepsilon_{z0}(z) + y \cdot \chi_x(z) - x \cdot \chi_y(z) \tag{2}$$

Where ε_{z0} is the membrane strain, χ_x and χ_y are the are the curvatures around the y and x axes. These quantities are denoted as section strains, collectively forming the section strain vector $\boldsymbol{e}(\boldsymbol{u})$:

$$\boldsymbol{e}(\boldsymbol{u}) = \left[\varepsilon_{z0}, \chi_x, \chi_y\right]^T \tag{3}$$

To reconstruct the displacement field from experimentally measured section strains, the least-square functional $\Phi^e(\boldsymbol{u}, \boldsymbol{e}_e^{\boldsymbol{\varepsilon}})$ is formulated for each element. It consists in the Euclidean norm of the error between the section strains according to the Euler-Bernoulli beam theory $\boldsymbol{e}^{\boldsymbol{e}}(\boldsymbol{u})$ and the experimentally measured strains $\boldsymbol{e}_{\boldsymbol{e}}^{\boldsymbol{\varepsilon}}$:

$$\Phi^e(\boldsymbol{u}, \boldsymbol{e}_e^{\boldsymbol{\varepsilon}}) = \|\boldsymbol{e}^{\boldsymbol{e}}(\boldsymbol{u}) - \boldsymbol{e}_{\boldsymbol{e}}^{\boldsymbol{\varepsilon}}\|^2 \tag{4}$$

The contributions of m inverse elements are then summed over in the functional Φ. The nodal displacements $\boldsymbol{u}$ are computed by minimizing the Φ.

$$\Phi = \sum_{e=1}^{m} \Phi^e(\boldsymbol{u}, \boldsymbol{e}_e^{\boldsymbol{\varepsilon}}) \tag{5}$$

The functional associated with the element can be expressed as:

$$\Phi^e(\boldsymbol{u}^{\boldsymbol{e}}, \boldsymbol{e}_e^{\boldsymbol{\varepsilon}}) = \sum_{k=1}^{3} w_k^e \cdot \Phi_k^e \tag{6}$$

Where w_k^e represents the k-th component of the weighting coefficient vector associated with the three components of the strain vector $\boldsymbol{e}(\boldsymbol{u})$. Specifically, $k = 1,2,3$ corresponds to the number of strain variables defined at a generic section of the element, which are used to describe the strain field. Therefore:

$$\begin{cases} \boldsymbol{w}^{\boldsymbol{e}} = \left[1, \dfrac{I_x^e}{A^e}, \dfrac{I_y^e}{A^e}\right] \\ \Phi_k^e = \dfrac{l^e}{n} \cdot \displaystyle\sum_{i=1}^{n} \left(e_{k_i}(\boldsymbol{u}^{\boldsymbol{e}}) - e_{k_i}^{\varepsilon}\right)^2 \end{cases} \tag{7}$$

Where l^e, A^e, I_x^e and I_y^e correspond to the length, cross-sectional area, and moments of inertia of the element, while n denotes the number of locations within the element where a sensor is installed to extract data (in this case, two sensors per element are considered, according to the 0[th] order element formulation [48]). The calculations for Φ_k^e are developed as follows:

$$\begin{aligned} \Phi_k^e &= \frac{l^e}{n} \cdot \sum_{i=1}^{n} \left((\boldsymbol{B}_k(z_i) \cdot \boldsymbol{u}^{\boldsymbol{e}})^2 - 2\boldsymbol{B}_k(z_i) \cdot \boldsymbol{u}^{\boldsymbol{e}} \cdot e_{k_i}^{\varepsilon} + \left(e_{k_i}^{\varepsilon}\right)^2 \right) \\ &= \frac{l^e}{n} \cdot \sum_{i=1}^{n} \left(\boldsymbol{u}^{\boldsymbol{e}^T} \cdot \boldsymbol{B}_k^T(z_i) \cdot \boldsymbol{B}_k(z_i) \cdot \boldsymbol{u}^{\boldsymbol{e}} - 2\boldsymbol{u}^{\boldsymbol{e}^T} \cdot \boldsymbol{B}_k^T(z_i) \cdot e_{k_i}^{\varepsilon} + e_{k_i}^2 \right) \end{aligned} \tag{8}$$

Where the matrix $\boldsymbol{B}_k(z_i)$ contains the derivatives of the shape functions [56].
Let us denote by $\boldsymbol{K^e}$ the stiffness matrix of the element and by $\boldsymbol{h^e}$ the vector containing the known curvature and membrane strain values. These can be defined as follows, according to the formulation described above:

$$\boldsymbol{K^e} = \frac{l^e}{n} \cdot \sum_{i=1}^{n} \boldsymbol{B}^T_{\varepsilon_{z0}}(z_i) \cdot \boldsymbol{B}_{\varepsilon_{z0}}(z_i) + \frac{l^e \cdot I^e_x}{n \cdot A^e} \cdot \sum_{i=1}^{n} \boldsymbol{B}^T_{\chi_x}(z_i) \cdot \boldsymbol{B}_{\chi_x}(z_i) + \frac{l^e \cdot I^e_y}{n \cdot A^e} \cdot \sum_{i=1}^{n} \boldsymbol{B}^T_{\chi_y}(z_i) \cdot \boldsymbol{B}_{\chi_y}(z_i) \tag{9}$$

$$\boldsymbol{h^e} = \frac{l^e}{n} \cdot \sum_{i=1}^{n} \boldsymbol{B}^T_{\varepsilon_z}(z_i) \cdot \varepsilon_{z0_i} + \frac{l^e \cdot I^e_x}{n \cdot A^e} \cdot \sum_{i=1}^{n} \boldsymbol{B}^T_{\chi_x}(z_i) \cdot \chi_{x_i} + \frac{l^e \cdot I^e_y}{n \cdot A^e} \cdot \sum_{i=1}^{n} \boldsymbol{B}^T_{\chi_y}(z_i) \cdot \chi_{y_i}$$

In this way, the element functional to be minimized can be written in its complete form as follows:

$$\Phi^e(\boldsymbol{u^e}, \boldsymbol{e^\varepsilon_e}) = \boldsymbol{u^{e^T}} \cdot \boldsymbol{K^e} \cdot \boldsymbol{u^e} - 2\boldsymbol{u^{e^T}} \cdot \boldsymbol{h^e} + c \tag{10}$$

To perform the minimization, the functional Φ^e can be differentiated with respect to $\boldsymbol{u^e}$ and set equal to zero. Knowing that the matrix $\boldsymbol{K^e}$ is symmetric, the following expression can therefore be written:

$$\frac{d\Phi^e}{d\boldsymbol{u^e}} = 2\boldsymbol{K^e} \cdot \boldsymbol{u^e} - 2\boldsymbol{h^e} = \boldsymbol{0} \tag{11}$$

Once all these quantities have been defined and $\boldsymbol{K^e}$ and $\boldsymbol{h^e}$ have been computed, the system can be transformed into global coordinates by applying an extraction matrix and a transformation matrix. The function to be minimized is now given by:

$$f(\boldsymbol{u}) = \frac{1}{2}\boldsymbol{u}^T \cdot \boldsymbol{K} \cdot \boldsymbol{u} - \boldsymbol{u}^T \cdot \boldsymbol{h} + c \tag{12}$$

The previous equation is expressed in global coordinates, so $\boldsymbol{u}$ is a vector of N degrees of freedom ($= 5 \cdot n_{nodes}$), while $\boldsymbol{h}$ is the vector containing the measured values of curvature and membrane strain and $\boldsymbol{K}$ is the stiffness matrix. Its solution becomes:

$$\boldsymbol{K} \cdot \boldsymbol{u} = \boldsymbol{h} \tag{13}$$

This can be solved by applying appropriate boundary conditions, which are necessary to invert the stiffness matrix. The next paragraphs are devoted to the strategies adopted for their implementation in the iFEM model.

2.2 Standard formulation for applying boundary conditions

Most commercial solvers developed to handle linear mechanical systems, such as those described by Eq. (13), rely on either the Lagrange Multipliers method for exact enforcement of boundary conditions or the Penalty method for their approximate enforcement. Both approaches require a priori knowledge of the mechanical characteristics of the structure under analysis. Two variants of Eq. (13)

can be formulated depending on the method employed to enforce the displacement boundary conditions.
In particular, the Lagrange Multipliers method leads to the following augmented linear system:

$$\begin{bmatrix} \boldsymbol{K} & \boldsymbol{V^T} \\ \boldsymbol{V} & \boldsymbol{0} \end{bmatrix} \begin{bmatrix} \boldsymbol{u} \\ \boldsymbol{\lambda} \end{bmatrix} = \begin{bmatrix} \boldsymbol{h} \\ \boldsymbol{u_{known}} \end{bmatrix} \tag{14}$$

Here, $\boldsymbol{V}$ is the constraint matrix, a sparse matrix with unit entries corresponding to the degrees of freedom subject to constraints. The vector $\boldsymbol{\lambda}$ contains the Lagrange multipliers, and $\boldsymbol{u_{known}}$ denotes the vector of prescribed displacements, while the matrix $\boldsymbol{K}$ and the vectors $\boldsymbol{u}$ and $\boldsymbol{h}$ have already been defined. Once the appropriate number of constraints is applied, the system can be solved to obtain both the displacement field $\boldsymbol{u}$ and the associated multipliers $\boldsymbol{\lambda}$.
On the other hand, the Penalty method leads to the following system of equations:

$$\begin{cases} \boldsymbol{K_{pen}} = \boldsymbol{K} + \boldsymbol{V} \cdot p \\ \boldsymbol{h_{pen}} = \boldsymbol{h} + \boldsymbol{a^T} \cdot p \\ \boldsymbol{u_{pen}} = \boldsymbol{K_{pen}^{-1}} \cdot \boldsymbol{h_{pen}} \end{cases} \quad with \;\; p \gg tr(\boldsymbol{K}) \tag{15}$$

In this formulation, p is the penalty coefficient, $tr(\boldsymbol{K})$ denotes the trace of the original stiffness matrix $\boldsymbol{K}$. The condition $p \gg tr(\boldsymbol{K})$ ensures that the constraint is effectively enforced. The vector $\boldsymbol{a}$ has the same dimension as $\boldsymbol{h}$, with non-zero values only at the degrees of freedom where displacements are prescribed; in those positions, $\boldsymbol{a}$ matches the known displacements.
Both the Lagrange multipliers and penalty methods require information about the displacements at the structural constraints to impose the corresponding boundary conditions in the system of equations. Specifically, these prescribed displacements are incorporated into the vectors $\boldsymbol{u_{known}}$ and $\boldsymbol{a}$, respectively, for the Lagrange multipliers and penalty formulations. In this study, the displacements or rotations associated with degrading boundary conditions are estimated by integrating the curvature field along the structure. The curvature field is derived from strain measurements as described in Eq. (2). For beam-type structures, the relationships between curvature, rotation, and vertical displacement can be expressed as:

$$\begin{cases} \varphi_x(z) = \varphi_x(z_0) + \int_{z_0}^{z} \chi_x(\eta)\, d\eta \\ v(z) = v(z_0) + \int_{z_0}^{z} \varphi_x(\eta)\, d\eta \end{cases} \tag{16}$$

Here, the variable η serves as a dummy variable of integration over the domain of the curvature and rotation functions. The term $\varphi_x(z)$ denotes the rotation field while $v(z)$ the vertical displacement field along the beam. The terms $\varphi_x(z_0)$ and $v(z_0)$ are known values of rotation and vertical displacement at a reference location z_0.
Hence, the correct identification of this reference point and its associated boundary values become essential. In the present work, only one end of the beam is assumed to undergo degradation (as detailed in Section 4). Consequently, z_0 corresponds to the ideal, non-degrading boundary condition—modeled as a perfectly clamped support with zero rotation and vertical displacement. Under this assumption, Eq. (16) becomes well-posed and can be solved to determine the rotation and vertical displacement at the degrading boundary.

Although the problem could be addressed more directly by installing displacement and rotation sensors at the degrading boundary—an approach that can be readily extended to scenarios involving multiple degrading supports—the curvature-integration method adopted here remains theoretically valid for the present experimental configuration. Moreover, it eliminates the need for additional sensors, thereby simplifying both the setup and the subsequent analysis process. Hence, any reference to prescribed displacements and $\boldsymbol{u_{meas}}$ in the following discussion pertains to values reconstructed from curvature integration, rather than to direct sensor measurements.
It should also be noted that Eq. (16) provides only an estimate of the imposed displacements at the degrees of freedom affected by boundary degradation. The iFEM method remains necessary to accurately reconstruct the complete displacement field, owing to its superior robustness and precision compared to direct integration, as demonstrated in [47]. It is also worth noting that the reliability of the strain-integration procedure fundamentally depends on a well-designed sensor network, which must provide strain measurements at appropriate locations and with sufficient spatial density to ensure an accurate curvature field for subsequent integration.
When the load is known to be a point load or a uniformly distributed load, Euler–Bernoulli theory gives the curvature a priori: linear for a point load, quadratic for a distributed load. Under mixed loading, the curvature can be expressed as a linear–quadratic combination with unknown coefficients identified by least squares on the measured strains.
Regarding constraint enforcement, in standard FEM Lagrange multipliers represent reactions and penalty terms approximate them. In iFEM, this physical meaning is lost because the matrices $\boldsymbol{K}$ and $\boldsymbol{h}$ are not the conventional stiffness and force vectors. Consequently, multipliers/penalty variables cannot be interpreted as actual reactions, and boundary stiffness cannot be recovered via $F = k_v \cdot v$ or $M = k_\varphi \cdot \varphi_x$. Beyond enforcing BCs, the goal is to identify time-varying boundary stiffness; thus we adopt a hybrid strategy tailored to iFEM rather than relying on classical reaction-based interpretations.

2.3 Hybrid direct-Lagrange method for equivalent stiffness estimation

Given the need for an alternative strategy, an alternative method is introduced, overcoming the limitations of classical reaction-based methods. A hybrid approach, combining the direct method [76]—in which virtual springs are introduced directly into the stiffness matrix at the boundary degrees of freedom— with the Lagrange Multipliers method, is used to address simultaneously: (i) the enforcement of known small displacements at the constrained nodes associated to degrading degrees of freedom and (ii) the identification of a stiffness parameter associated with each degree of constraint, which can be interpreted as a quantitative indicator of the constraint's integrity.
In this approach, the structure is modelled with linear spring elements at the boundary nodes associated with observable DOFs, effectively simulating flexible boundary conditions. These springs are compatible with the small displacement assumption underlying iFEM, which is not suited to capture geometric nonlinearities.
A key aspect of this approach is the distinction between observable and non-observable constrained degrees of freedom (DOFs). According to the case study presented in Section 4, where the sensors are placed exclusively on the bottom surface of the beam, only vertical displacement and rotation about the horizontal axis can be directly inferred from strain measurements (Figure 1).
Consequently:

- *Observable DOFs* are those that can be inferred from the available strain measurements—namely, the vertical displacement v and the rotation about the horizontal axis φ_x.

- *Non-observable DOFs* are those that cannot be directly reconstructed due to sensor placement, including the axial displacement w, horizontal displacement u, and rotation about the vertical axis φ_y.

To avoid issues related to ill-conditioning of the system and to ensure exact enforcement of zero displacement, the non-observable constrained degrees of freedom are fixed using the Lagrange Multipliers method. This prevents spurious or misleading displacement artifacts from propagating into the vertical plane, where the actual sensor data is used for reconstruction, thereby preserving the reliability of the computed displacements for the observable degrees of freedom.

For the observable degrees of freedom, equivalent stiffness coefficients are introduced at the corresponding diagonal entries of the matrix $\boldsymbol{K}$, thereby modeling the contribution of virtual springs attached to the ground. This approach, known as the direct stiffness method, is used to assemble global FEM stiffness matrices [78], allows for both the approximate enforcement of displacement constraints and the estimation of stiffness values at the boundaries. Since these springs are assumed to be grounded, no relative displacement occurs at their base. The proposed approach leads to the following augmented system:

$$\begin{bmatrix} \boldsymbol{K}(k_{ii}) & \boldsymbol{C^T} \\ \boldsymbol{C} & \boldsymbol{0} \end{bmatrix} \begin{bmatrix} \boldsymbol{u} \\ \boldsymbol{\lambda} \end{bmatrix} = \begin{bmatrix} \boldsymbol{h} \\ \boldsymbol{0} \end{bmatrix}, \quad i \in observable\ DOFs \tag{17}$$

Here, $\boldsymbol{C}$ is the constraint matrix, like $\boldsymbol{V}$ in Eq. (14), but containing unit entries only at the locations corresponding to the non-observable constrained degrees of freedom. The vector $\boldsymbol{\lambda}$ contains the Lagrange Multipliers associated with these non-observable constraints, while k_{ii} represents the equivalent stiffness coefficients of the virtual springs associated with the observable constrained degrees of freedom. Accordingly, the matrix $\boldsymbol{K}(k_{ii})$ is modified as:

$$\boldsymbol{K}(k_{ii}) = \boldsymbol{K} + k_{ii} \cdot \boldsymbol{E}_{ii}\,, \quad i \in observable\ DOFs \tag{18}$$

In this expression, $\boldsymbol{E}_{ii}$ is a matrix with a single nonzero entry equal to 1 at position (i, i) and zeros elsewhere. The optimal values of k_{ii} in Eq. (17) and Eq. (18) are determined through numerical optimization, which minimizes the following residual function:

$$r(\boldsymbol{u}, k_{ii}) = \|\boldsymbol{O} \cdot \boldsymbol{u}(k_{ii}) - \boldsymbol{u_{meas}}\|^2, \quad i \in observable\ DOFs \tag{19}$$

Where $\boldsymbol{O}$ is a sparse selection matrix with unit entries corresponding to the observable constrained degrees of freedom, and $\boldsymbol{u_{meas}}$ is the vector of prescribed displacements at those degrees of freedom. These displacements are derived from curvature integration, as detailed in Section 2.2. It is important to emphasize that $\boldsymbol{u}(k_{ii})$ does not correspond to the displacement field reconstructed by the iFEM procedure. Instead, it represents the displacement response of the structural system, parameterized by the unknown stiffness coefficient k_{ii}, and obtained through the inversion of the augmented system in Eq. (17). The computation of $\boldsymbol{u}(k_{ii})$ remains intrinsically linked to the iFEM formulation, since both the matrix $\boldsymbol{K}$ and the vector $\boldsymbol{h}$ are derived from the iFEM equations. The optimization process seeks the value of k_{ii} that minimizes the discrepancy between the displacement predicted by this model and the prescribed displacement, as defined by the residual function in Eq. (19). Because the displacement vector $\boldsymbol{u}(k_{ii})$ is implicitly dependent on k_{ii} through the matrix inversion, the residual function exhibits a nonlinear dependence on the boundary stiffness. Consequently, solving for k_{ii} requires an iterative numerical procedure.

The function is formulated in a least-squares sense to exploit efficient optimization algorithms available in MATLAB's *Optimization Toolbox*. Specifically, the Trust-Region Reflective algorithm

[79, 80] is employed for its suitability in handling constrained optimization problems with upper and lower limits on the parameters to be estimated. In this context, the parameters k_{ii} must remain within reasonable ranges: if too large relative to the entries of the matrix $\boldsymbol{K}$, the system becomes ill-conditioned; if too small, the springs are ineffective, potentially leading to rigid body motions and indistinguishable solutions across configurations. To balance numerical stability and physical effectiveness, a range of $0 < k_{ii} < 1$ has been selected.

2.4 Boundary condition degradation evaluation

In this work, the percentage variation of boundary stiffness is adopted as a quantitative indicator of the degree of degradation occurring at the constraints. This measure offers a direct and interpretable insight into the mechanical integrity (and so degradation) of the support conditions. To evaluate degradation, three methods are introduced, distinguished by the level of prior knowledge available about the material and structural properties.
Specifically, we classify the methods by two factors: whether the structure's elastic modulus E is known and assumed time-invariant, and whether the constraint's initial (undegraded) stiffness is known. The combination of these conditions defines three progressively general approaches, which are described in the following sections.

2.4.1 Rotational degree of degradation with known material properties

If the elastic modulus E is known and assumed to be constant over time, it is possible to compute the absolute stiffness of the constraints using the Euler-Bernoulli beam equation, which forms the theoretical foundation of the iFEM framework described in Section 2.1, in combination with the governing equation of a spring element. The following relationships apply:

$$\begin{cases} M(z_i) = -\dfrac{d^2v(z_i)}{dz^2} \cdot EI \\ M(z_i) = k_\varphi \cdot \varphi_x(z_i) \end{cases} \tag{20}$$

Here, z_i denotes the location of the constraint in the structure, where the reaction moment M, curvature $-\frac{d^2v}{dz^2}$, and the rotation φ_x are evaluated. The curvature is computed from Eq. (2) after the collection of strain measurements, while the rotation is computed solving Eq. (13). From these quantities, the spring stiffness can be calculated. Given the stiffness values $k_{\varphi,estimated_t}$ and $k_{\varphi,estimated_{t+1}}$ at two different time instants, the degree of degradation can be expressed as:

$$\Delta k_{\varphi_{\%,estimated}} = -\left(\frac{k_{\varphi,estimated_t} - k_{\varphi,estimated_{t+1}}}{k_{\varphi,estimated_t}}\right) \cdot 100 \tag{21}$$

This equation gives the percentage stiffness drop between two consecutive instants. If the original stiffness is known, degradation can be referenced to the structure's initial condition. Its key benefit is that it returns stiffness to physical units, enabling direct structural analyses: residual stiffness quantifies remaining capacity and supports choosing retrofit actions to restore boundary performance.

2.4.2 Rotational degree of degradation with unknown material properties but known initial stiffness

This approach eliminates the need for known material properties, except for the assumption that the flexural rigidity EI remains constant over time. This assumption is reasonable only for structures not subject to significant material degradation, as for the method described in Section 2.4.1. The method relies solely on kinematic quantities obtained from sensor data, solving Eq. (2) and Eq. (13) and follows the Euler-Bernoulli beam formulation. From Eq. (20), the stiffness at two different instants can be written as:

$$\begin{cases} k_{\varphi_t} = -\dfrac{\chi_{x_t}}{\varphi_{x_t}} EI \\ k_{\varphi_{t+1}} = -\dfrac{\chi_{x_{t+1}}}{\varphi_{x_{t+1}}} EI \end{cases} \tag{22}$$

The relative change in stiffness is then given by:

$$\Delta k_{\varphi_{\%,estimated}} = -\left(1 - \frac{\chi_{x_{t+1}}}{\chi_{x_t}} \cdot \frac{\varphi_{x_t}}{\varphi_{x_{t+1}}}\right) \cdot 100 \tag{23}$$

It relies solely on kinematic measurements—typically easier to acquire—but yields only relative stiffness changes. To obtain absolute stiffness $k_{estimated_t}$ at time t, one must know the initial (healthy) stiffness $k_{healthy}$ from design or simulation; the relative variation is then scaled for structural analyses (e.g., reinforcement design). The relation is:

$$k_{estimated_t} = k_{healthy} \cdot \left(1 + \frac{\Delta k_{\varphi_{\%,estimated}}(0 \to t)}{100}\right) \tag{24}$$

Here, $\Delta k_{\varphi_{\%,estimated}}(0 \to t)$ represents the percentage change in stiffness between the initial state (0) and the current time t, computed from Eq. (23). These are compared against the initial values associated with the known stiffness $k_{healthy}$. Nonetheless, this requirement may limit the applicability of the method in cases where the original boundary conditions are unknown or difficult to estimate.

2.4.3 Rotational degree of degradation with unknown material properties and initial stiffness

If neither material properties nor initial stiffness are known, degradation can still be assessed by estimating equivalent stiffness via the optimization in Eq. (19). values k_{iFEM_t} and $k_{iFEM_{t+1}}$, the percentage drop follows Eq. (21), yielding $\Delta k_{\varphi_{\%,iFEM}}$. This needs only the iFEM model and identification step; a calibration/reference is then required to map k_{iFEM} to physical units for structural use (e.g., retrofit design). See Section 5 for details.

2.4.4 Vertical degree of degradation

While the Euler–Bernoulli beam theory neglects shear deformation, the internal shear force $T(z_i)$ defined as the derivative of the bending moment with respect to the beam axis, remains a valid equilibrium quantity:

(25)

$$T = \frac{dM}{dz} = \frac{d\chi_x}{dz} EI$$

This quantity can be exploited to assess the degradation of constraints that produce vertical displacements, using any of the three previously described methods. At a constrained location z_i, the reaction shear force can be interpreted as being transmitted through a vertical translational spring with stiffness k_v, such that:

$$T(z_i) = k_v \cdot v(z_i) \tag{26}$$

where $v(z_i)$ is the vertical displacement at the constraint, reconstructed by the iFEM algorithm.
These two expressions can be combined to evaluate the vertical stiffness and its evolution over time, similarly to the method discussed in Section 2.4.1. In analogy with Eq. (23), the percentage degradation in vertical stiffness can be expressed also as:

$$\Delta k_{v\%,estimated} = -\left(1 - \frac{\left(\frac{d\chi_x}{dz}\right)_{t+1}}{\left(\frac{d\chi_x}{dz}\right)_t} \cdot \frac{v_t}{v_{t+1}}\right) \cdot 100 \tag{27}$$

This formulation relies entirely on kinematic quantities and requires only the derivative of the curvature at the constraint, in addition to the displacement, both obtainable from sensor data.
If material properties are unknown, the procedure in Section 2.4.3 can be followed, using the estimated equivalent stiffness coefficients corresponding to the vertical degrees of freedom at the constraint locations.
This extension complements the rotational degradation analysis and enables a complete characterization of the constraint's effectiveness over time.

3. Research framework methodology

Figure 2 schematizes the 1D iFEM-based framework developed to reconstruct the displacement field and boundary stiffness in the presence of degrading boundary conditions in real case scenarios.

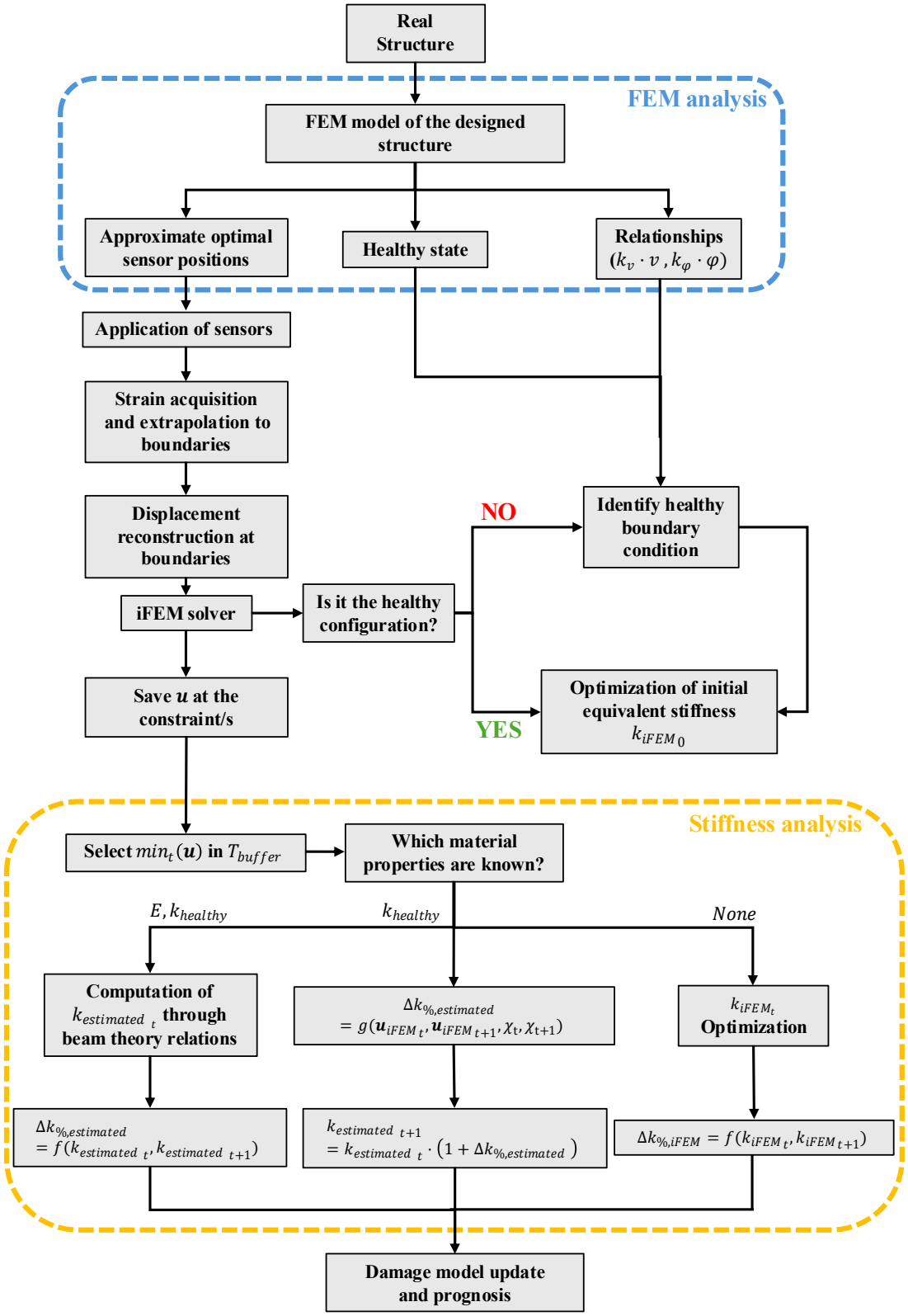

Figure 2 Workflow chart of the framework implemented in the presented research.

The proposed methodology for identifying and monitoring degradation in structural boundary conditions involves the following steps:

- Selection of the monitored structure: Choose a real structure (e.g., a bridge girder or a frame beam) with boundary conditions prone to degradation—either new or in service—and design the monitoring system to track boundary behavior over time.
- Development of a reference FEM model: Build a direct FEM model using geometry, materials, and code-based loads to represent the healthy state. It (i) provides a baseline to detect displacement/stiffness deviations due to boundary degradation and (ii) supports optimal sensor placement.
- Design and deployment of the sensor network: Install an FBG-based sensor network at selected locations, considering expected loads and environmental conditions. The network captures the strain data required for real-time structural analysis.
- Boundary generalized displacements estimation: Use continuously measured strains as iFEM inputs for real-time displacement/strain reconstruction. When actual BCs deviate from design, iFEM may fail; thus, it is possible to estimate boundary kinematics—rotation for degraded clamps or vertical settlement for degraded vertical supports—directly from measured strains in real time, following Eqs. (2) and (16).
- Shape sensing: The estimated boundary kinematics are then imposed in the iFEM model to improve shape-sensing under degraded BCs. For each originally constrained DOF (e.g., fixed displacement or rotation), the constraint is relaxed and replaced by the corresponding imposed displacement or rotation.
- Initial equivalent stiffness estimation: If the reconstructed displacement field and estimated boundary kinematics deviate from the healthy (design) state, the original boundary conditions are re-identified. An optimization (Section 2.3) yields the initial equivalent stiffness k_{iFEM_0}, which serves as a baseline to quantify degradation.
- Isolation of load effects on the boundary displacements: The estimated boundary rotation/settlement reflects both true degradation and external loads, so larger loads can bias the equivalent stiffness to appear smaller (or vary across updates) without any real recovery/loss. To decouple loading, at each stiffness-update interval $\Delta t_{stiffness}$), it is possible to consider a preceding buffer window T_{buffer} (e.g., 24 h). Because degradation evolves slowly, real-time estimation is unnecessary. Within T_{buffer}, it is possible to track the boundary rotation/displacement and take its minimum as a proxy for the unloaded state. This value—attributed to degradation only—is then used to estimate the equivalent stiffness coefficients.
- Stiffness analysis: After removing load effects, stiffness is evaluated based on available information (elastic modulus and initial boundary stiffness), with three cases:
  - Case A → E and initial constraint stiffness known: Apply beam theory (e.g., Eq. (20)) to compute the current stiffness in physical units; quantify degradation via the percentage change in Eq. (21).
  - Case B → Only initial stiffness known. If E is unknown but time-invariant, manipulate Eq. (20) to express percentage degradation using kinematic quantities; recover absolute stiffness afterward via Eq. (24).
  - Case C → Neither E nor initial stiffness known. Solve the nonlinear system in Eq. (19) to identify the equivalent stiffness coefficients k_{ii} (embedded in the iFEM matrix $\boldsymbol{K}$) for the degrading DOFs. Compute the percentage change with Eq. (21) relative to the reference (healthy) value k_{iFEM_0}. For new structures, obtain k_{iFEM_0} from early strain data post-commissioning; for in-service structures, infer the original stiffness as producing a boundary

rotation/displacement equal to 1% of the maximum allowable at the degraded DOF, via FEM. Because k_{TARGET_0} (FEM) and k_{iFEM_0} differ in units/meaning, establish a priori mapping through FEM simulations to convert between equivalent and real stiffness. This also overcomes the FEM limitation where ideal BCs (clamped/simply supported) imply numerically inadmissible infinite stiffness, yielding a practical, stable definition of the healthy boundary stiffness.

- Degradation model update and prognosis: With boundary stiffness estimates available at multiple instants, we perform model updating on a chosen degradation law (physical or empirical). Parameters are identified online via sequential Bayesian estimation (e.g., particle filters), assimilating new sensor data to refine the posterior over time. The updated model then supports prognostics—predicting boundary deterioration at intervals $\Delta t_{stiffness}$ and assessing performance implications—thereby informing maintenance scheduling, safety evaluation, and life-cycle management.

4. Case study

The proposed framework was validated through an experimental investigation on an aluminum beam, considering different types and levels of boundary condition degradation. This section introduces the case studies: in particular, the specimen and the experimental set up are described in Section 4.1, the experimental tests are described in Section 4.2, the sensor network is described in Section 4.3, and the developed iFEM model is presented in Section 4.4.

4.1 Specimen and experimental setup

For this study, a simple experimental aluminum beam was considered, characterized by a rectangular cross-section measuring $50\,mm$ in width and $10\,mm$ in height, with a support span L of $648\,mm$ (Figure 3). The material properties assigned to the aluminum were a Young's modulus $E = 69\,GPa$ and Poisson's ratio $\nu = 0.3$, as provided by the supplier's datasheet. A static load scenario was considered, consisting of a single concentrated force applied at midspan with a magnitude of $F = 294.3\,N$, equivalent to the force exerted by a $30\,kg$ mass. The beam was mounted on a rigid steel frame, designed such that its own deformation under load would be negligible in comparison to the deformation of the test beam itself. Two aluminium spacer blocks were fixed between the beam, and the steel frame supports. These blocks raised the beam's height, enabling the three mechanical comparators to measure vertical displacements at selected points along the beam. These measurements served as a primary benchmark for validating the displacement fields reconstructed by the iFEM. The experiments begin with clamped boundary conditions, implemented by fastening the beam to spacer blocks using four bolts on each side. The solutions for the progressive degradation processes are then detailed in Section 4.2, while the experimental setup is shown in Figure 3.

(a) (b)

Figure 3 Experimental setup: (a) Overview of the beam with the total span *L* highlighted; (b) view of the applied load at midspan, consisting of a steel weight suspended by a steel cable.

FBG sensors were mounted on the beam's bottom surface centerline (as described in Section 4.3) to capture in-plane behavior. Strain was acquired with an HBM DI410 optical interrogator using Fabry–Perot tunable filter technology and catman® Easy/AP control.

4.2 Experimental static tests

Two boundary-degradation scenarios were analyzed—rotational degradation and vertical settlement—tested separately. Only the left support was allowed to degrade, while the right remained fully clamped (Figure 4). Degradation was modeled as a progressive loss of constraint effectiveness over service life.

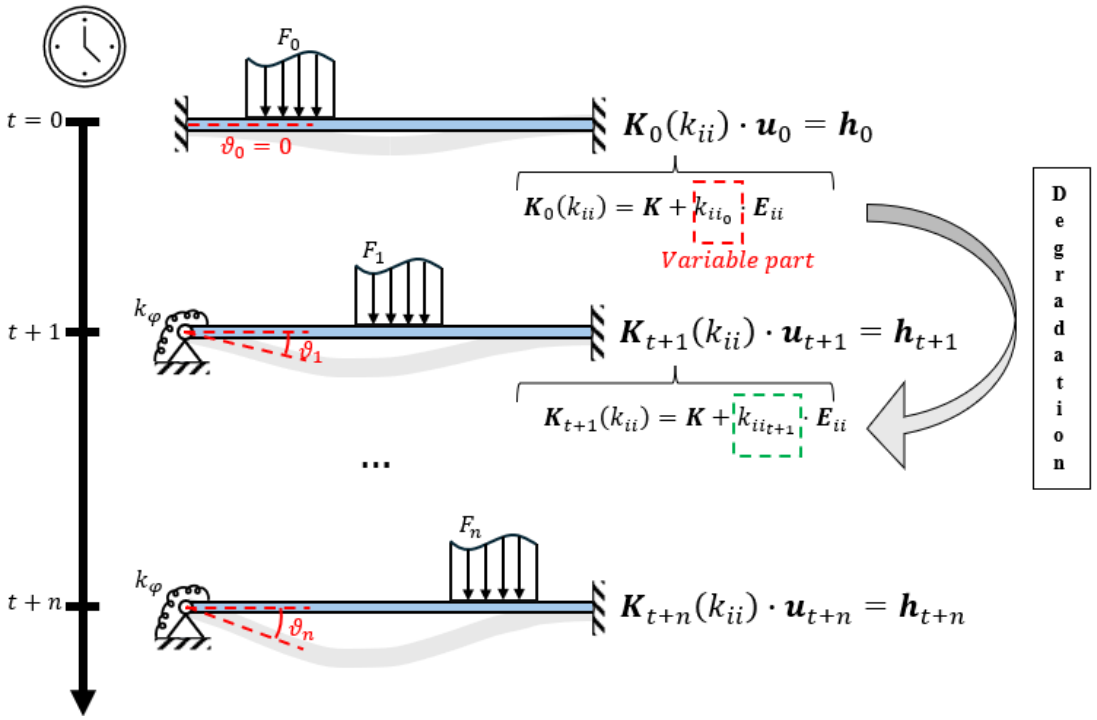

(a)

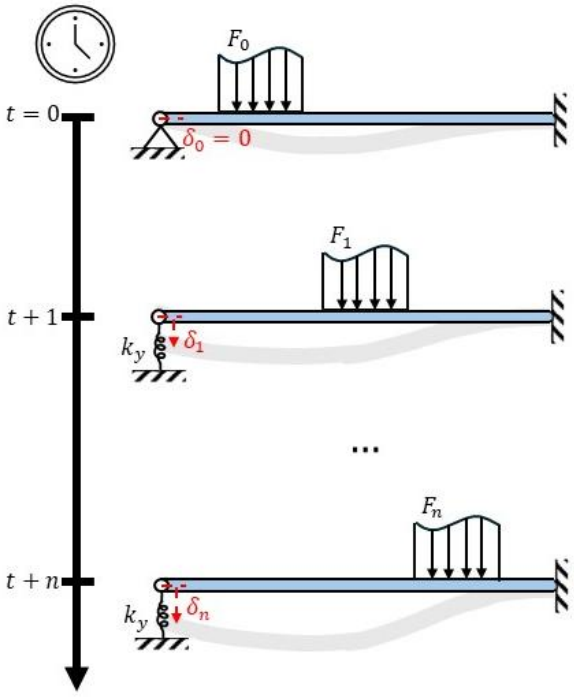

(b)

Figure 4 Schematic representation of the two classes of boundary condition degradation: (a) model with rotational degradation and illustration of the updated system of equations as explained in Section 2; (b) model with vertical displacement degradation.

Seven levels were defined from FEM predictions at the fully degraded limit: a pinned left support for rotational degradation (maximum rotation $0.01324\,rad$) and a free end for vertical settlement (maximum vertical displacement $28.60\,mm$). To remain within small-displacement assumptions ($\approx$ commonly set to $\frac{1}{100}$ of the beam length L) and avoid spring nonlinearity, the adopted levels were: rotation at 1%, 5%, 10%, 20%, 30%, 40%, 50% of the maximum; vertical settlement at 1%, 1.5%, 2%, 5%, 10%, 12%, 15% of the maximum. Beyond 50% and 15% respectively, the boundary was deemed functionally ineffective (realistic failure assumption in practical applications).
In the absence of a device capable of precisely imposing the required boundary displacement or stiffness, two scenario-specific procedures were implemented.
For rotational degradation, FE analyses were first conducted to determine the target stiffness k_{TARGET} and the corresponding strain field under the prescribed load and boundary displacement. In the experiment, the bolts at the left support were progressively loosened until the measured strain matched the FEM prediction, thereby reproducing the desired degradation level.
For vertical settlement, seven spacer plates ($50 \times 50 \times 10$ mm³) were fabricated via fused deposition modeling (Bambu Lab P1S printer) using thermoplastic polyurethane, each plate exhibiting a distinct compressive stiffness k_{TPU} (initial force–displacement slope), so that $k_{TARGET} = k_{TPU}$. The plates were inserted between the beam end and the aluminum support block to vary vertical compliance; replacing a plate with modified the local boundary stiffness and the associated displacement response (Figure 5).
For each configuration, strain measurements were acquired and processed as described in Section 3 to obtain vertical-plane displacements, the equivalent stiffness k_{iFEM}, and the corresponding degree of boundary degradation.

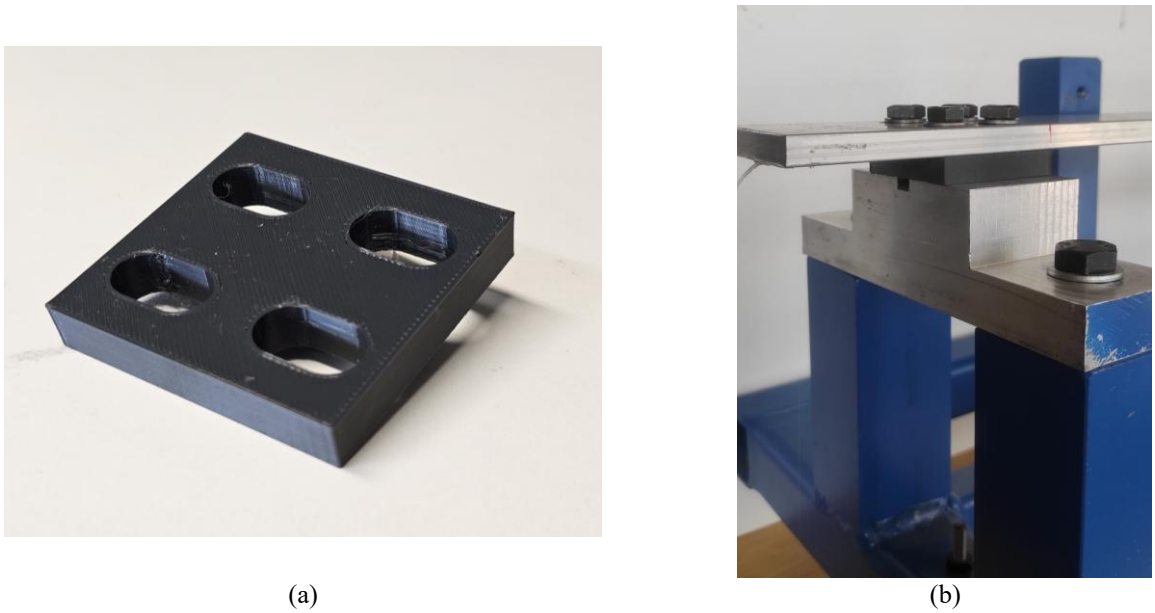

(a) (b)

Figure 5 Degraded boundary condition for the vertical displacement class: (a) additive manufactured spacer plate; (b) spacer plate applied to the structure's boundary condition.

4.3 The sensor network and its installation

An FBG-based sensor network was used (see Figure 6 and Figure 7). The network includes 18 sensing points spaced at $36\,mm$. FBGs reflect a specific Bragg wavelength that shifts with strain, enabling

accurate strain measurements. To prevent spectral overlapping between adjacent sensors, we satisfied the manufacturer's spacing condition [81]:

$$\varepsilon_{max} \ll \frac{\Delta\lambda}{\lambda \cdot s} \tag{28}$$

Where ε_{max} is the maximum expected measured strain in the beam, $\Delta\lambda$ is the wavelength range available per sensor, calculated by dividing the total wavelength range of the fiber (in this case, $1520 - 1580\ nm$) by the number of sensors, and rounding to the nearest integer. λ is conventionally set to the central wavelength of the total range, therefore $1550\ nm$. s is the strain sensitivity at room temperature provided by the manufacturer as $7.8 \cdot 10^{-7} \mu\varepsilon^{-1}$. The sensor wavelengths shown in Figure 6 were selected based on Eq. (28) to ensure that the expected strain remained well below the threshold where spectral overlap may occur.

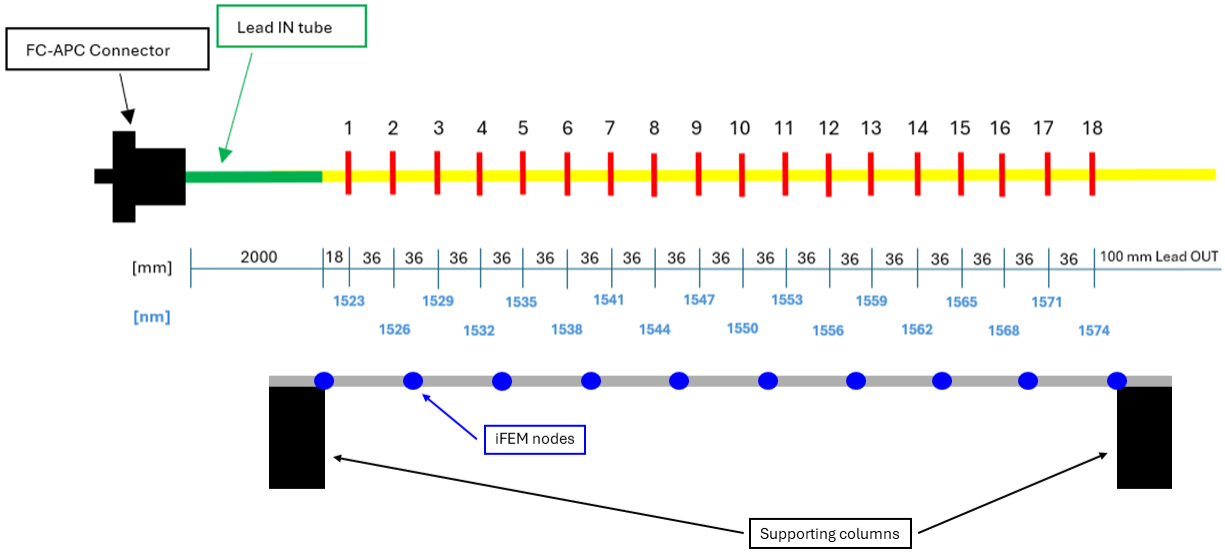

Figure 6 FBG-based sensor network layout and representation of the nodes of the iFEM model with 9 inverse elements. Each inverse element contains 2 sensors.

Figure 7 Installed sensor network on the beam (black line on the bottom surface).

4.4 The iFEM model

The iFEM model developed for the experimental case consists of a number of inverse finite elements whose quantity is directly determined by the number and positions of the installed strain sensors. Based on the adopted sensor network, three discretization were possible, corresponding to models with 3, 6, or 9 inverse elements. This flexibility arises from the type of element employed in the formulation, which, as described in Eq. (7), requires two strain input locations per element. These so-called input strain locations represent the points where membrane strain and curvature, derived from the extracted measured strain, are assigned within each element.

As discussed in Section 2, only the geometric properties need to be specified: the cross-sectional area, the moment of inertia, and the element length. All these parameters are kept constant throughout the beam, as no geometric or material discontinuities are present in the experimental setup. Since the physical positions of the sensors along the optical fiber, and consequently along the beam, are fixed, changing the number of elements modifies the length of each element and the relative placement of the input strain locations within it. For the configurations with 3, 6, and 9 elements, the input strain positions correspond to $\frac{5}{12}$ and $\frac{9}{12}$, $\frac{1}{6}$ and $\frac{5}{6}$, and finally $\frac{1}{4}$ and $\frac{3}{4}$ of the element length, respectively.

It is important to highlight that the 3-element configuration lacks symmetric input strain locations with respect to the midpoint of the element. This asymmetry introduces a source of approximation error, especially where the strain function changes sign, typically at the point of force application. As a result, greater errors can emerge in the reconstructed displacement field, as further discussed in Section 5.1.

Another key consideration is that the current iFEM formulation, presented in Section 2.1, is especially well suited for reconstructing strain distributions resulting from concentrated loads. Within the framework of Euler-Bernoulli beam theory, the strain distribution is linear under such loading, and two measurement points per element are sufficient to accurately capture this behavior. However, if the beam is subjected to more complex load conditions, such as distributed loads, the strain distribution becomes nonlinear, and the current formulation provides an approximation only.

5. Results and discussion

The experimental data acquired in the case study described in Section 4 were analyzed to assess the effectiveness and performance of the proposed method. Specifically, Section 5.1 presents a sensitivity analysis on the inverse mesh size; Section 5.2 discusses the results for the scenario of rotational boundary condition degradation; and finally, Section 5.3 examines the results for the scenario of vertical displacement boundary condition degradation.

5.1 Inverse mesh sensitivity analysis

As already mentioned, the sensor network described in Section 4.3 enabled the development of three iFEM meshes, composed of 3, 6, or 9 inverse elements, as explained in Section 4.4. Figure 8 illustrates the vertical displacements reconstructed provided by the iFEM considering three mesh configurations, applied to the healthy structure modeled with fully clamped boundary conditions at both ends. The reconstructed displacement field is compared with the analytical solution provided by Euler-Bernoulli beam theory and with the displacement values recorded by the three dial gauges (positioned respectively at z coordinate equal to $L/4$, $L/2$ and $2L/3$.

Increasing the number of elements improves reconstruction via finer discretization and more symmetric strain inputs. The 3-element mesh, lacking symmetry, shows reduced accuracy—highlighting the importance of sensor placement. With 6 and 9 elements, displacements agree well with the analytical solution, and iFEM predictions also match the three dial-gauge measurements.

To gain a comprehensive view of the iFEM performance, the performance metrics reported in Table 1 highlight more evident differences between iFEM and analytical calculation. These metrics include the absolute maximum error (AME, $\mathrm{AME} = \max_i \left| v_i^{iFEM} - v_i^{analytical} \right|$), the mean percentage difference (MPD, $\mathrm{MPD} = \frac{100}{N} \cdot \sum_{i=1}^{N} \left| \frac{v_i^{iFEM} - v_i^{analytical}}{v_i^{analytical}} \right|$), and the root mean square error (RMSE, $\mathrm{RMSE} = \sqrt{\frac{1}{N} \cdot \sum_{i=1}^{N} \left(v_i^{iFEM} - v_i^{analytical} \right)^2}$). It is important to note that these comparisons are made against the analytical solution, as the dial gauges provide displacement measurements at only three discrete points. Therefore, to evaluate reconstruction accuracy along the entire beam length, the analytical solution serves as reference. A total of 649 points (N) were considered along the beam (one point per millimeter) for the previous comparisons.

Notably, the 6-element mesh outperforms the 9-element one because a node coincides with the load point, boosting local reconstruction accuracy. In the 9-element mesh, the load falls mid-element, adjacent sensors read nearly the same strain, and curvature near the force is under-resolved, yielding small displacement errors. When the load location is known, align an iFEM node with it; when uncertain (as in practice), increasing the number of inverse elements generally improves accuracy by refining spatial resolution.

For the analysis of boundary condition degradation, the mesh with 6 elements was selected, as the load application point is known as a priori from the mass positioning on the experimental beam. This makes it the most suitable configuration for the study. In real-world applications, however, the optimal sensor network should be identified through preliminary analyses—for instance, by using numerically computed strain fields to guide sensor placement.

The same performance patterns and metric trends were also confirmed in the second configuration with ideal support–clamp boundary conditions. For the sake of brevity, these results are omitted from the present discussion.

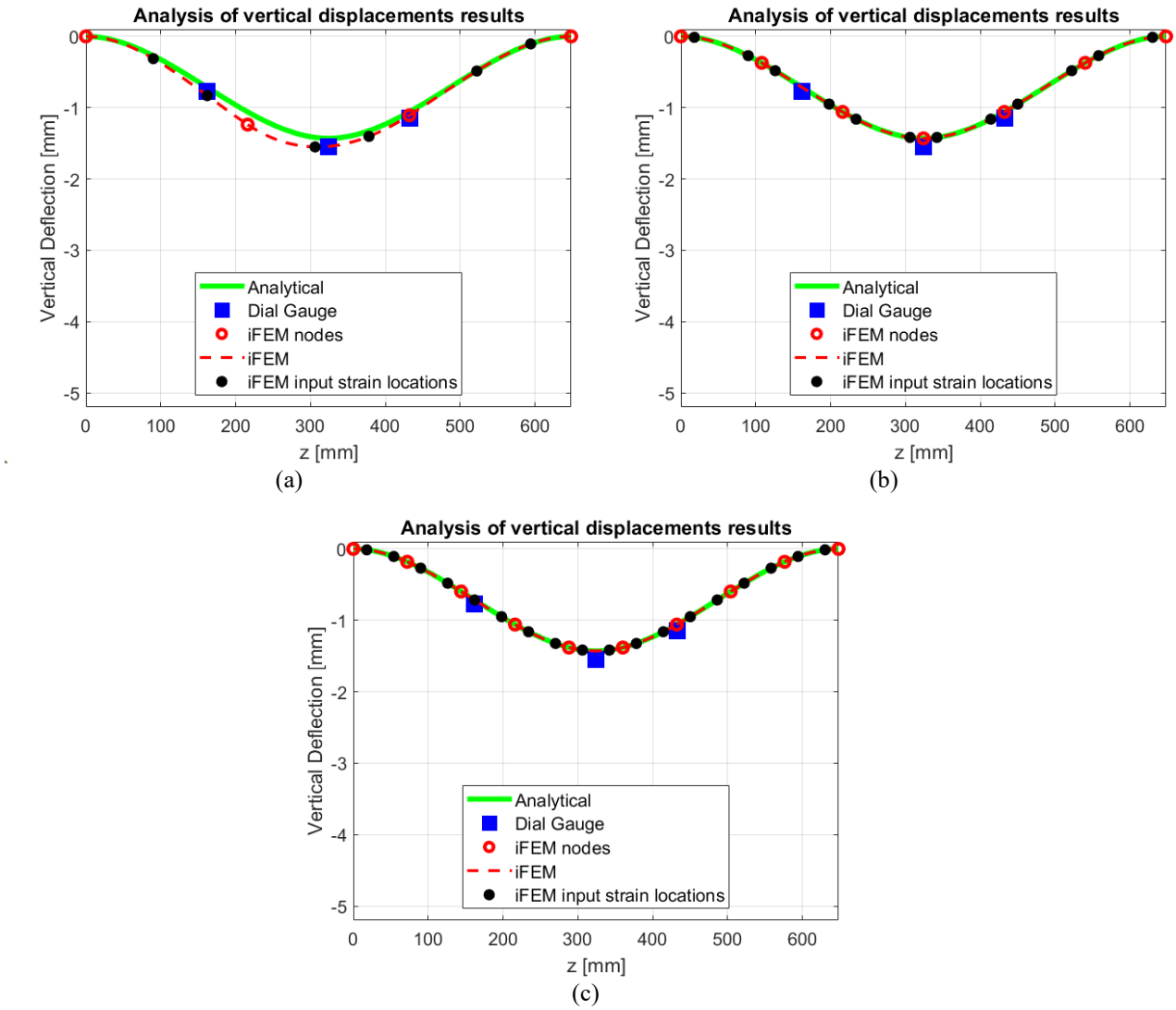

Figure 8 Mesh sensitivity analysis on the healthy configuration of the beam. Reconstructed vertical displacements using: (a) 3 inverse elements; (b) 6 inverse elements; (c) 9 inverse elements.

Table 1 Performance metrics for iFEM meshes with 3, 6, and 9 elements on the healthy beam configuration (double clamp boundary condition and concentrated 30 kg force at the midpoint).

N° elements	AME $[mm]$	MPD [%]	RMSE $[mm]$
3	0.19	8.89	0.0913
6	0.00000112	0.0000164	0.000000493
9	0.00196	0.00765	0.000398

5.2 Rotational degradation analysis

This section examines rotational boundary-condition degradation. Although several levels were tested (Section 4.2), figures show two representative cases; all levels are included in the results and discussed in the analysis.

Figures 9, 10, and 11 show the reconstructed displacements, rotations, and bottom surface strains, respectively, for two degradation levels corresponding to 10% and 50% of the maximum allowed rotation ($0.01324\ rad$), as detailed in Section 4.2. The imposed rotations at the degrading boundary condition for accurate shape sensing purposes are $0.001324\ rad$ for degradation level equal to 10%

and $0.00662\ rad$ for degradation level equal to 50%. From the figures, it is evident that the two degradation levels are clearly distinguishable, yet the iFEM model successfully reconstructs the structural behavior in both cases, yielding MPD metric values below 1%. Notably, as the degradation increases, the strain distribution adapts accordingly: strain values decrease near the degrading boundary and increase near the non-degrading boundary. This trend is consistent with a shift in the bending behavior (Figures 11), where reduced stiffness at the degraded end leads to increased bending and strain on the opposite, non-degraded side, as also visible from the deformed shape in Figure 9.
Regarding the estimation of the equivalent rotational stiffness coefficients for different degradation levels, the conducted analysis resulted in the outcomes presented in Table 2 and Table 3. These tables include the equivalent stiffness coefficients k_{iFEM}, the corresponding reference stiffness values obtained from FEM simulations k_{TARGET} and the degree of degradation $\Delta k_{\varphi_{\%}}$, computed as described in Section 2.4. To accurately evaluate $\Delta k_{\varphi_{\%}}$, the reference stiffness value for the healthy configuration (k_{TARGET_0}) was extracted from a FEM simulation, as detailed in Section 3 (see case C).

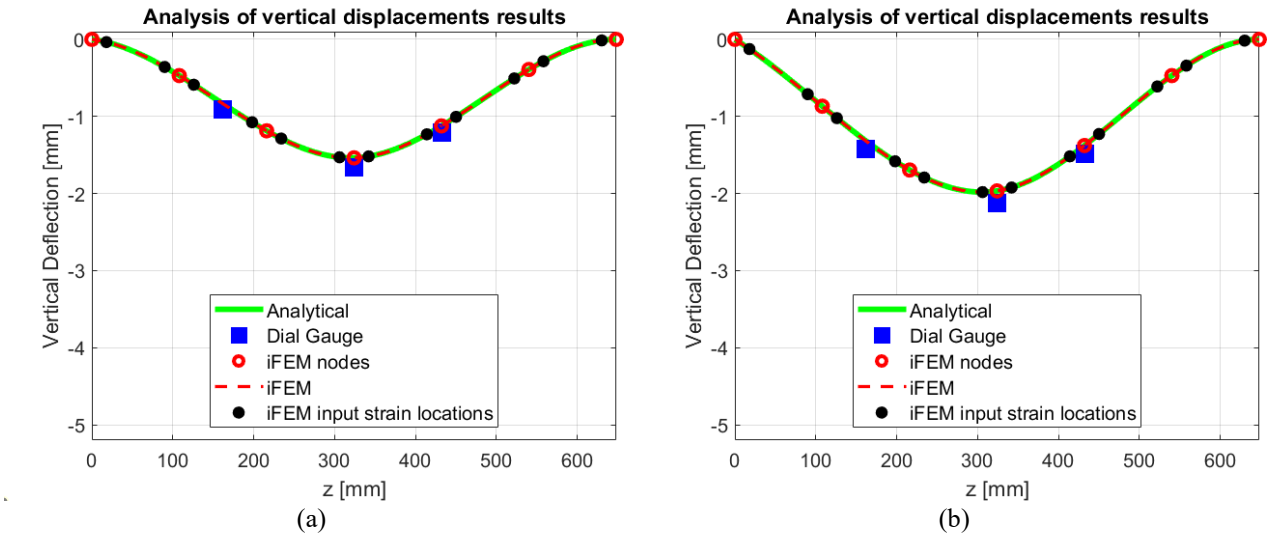

Figure 9 Reconstructed vertical displacements for the beam with a degrading rotational boundary condition at the left end: (a) 10% degradation; (b) 50% degradation.

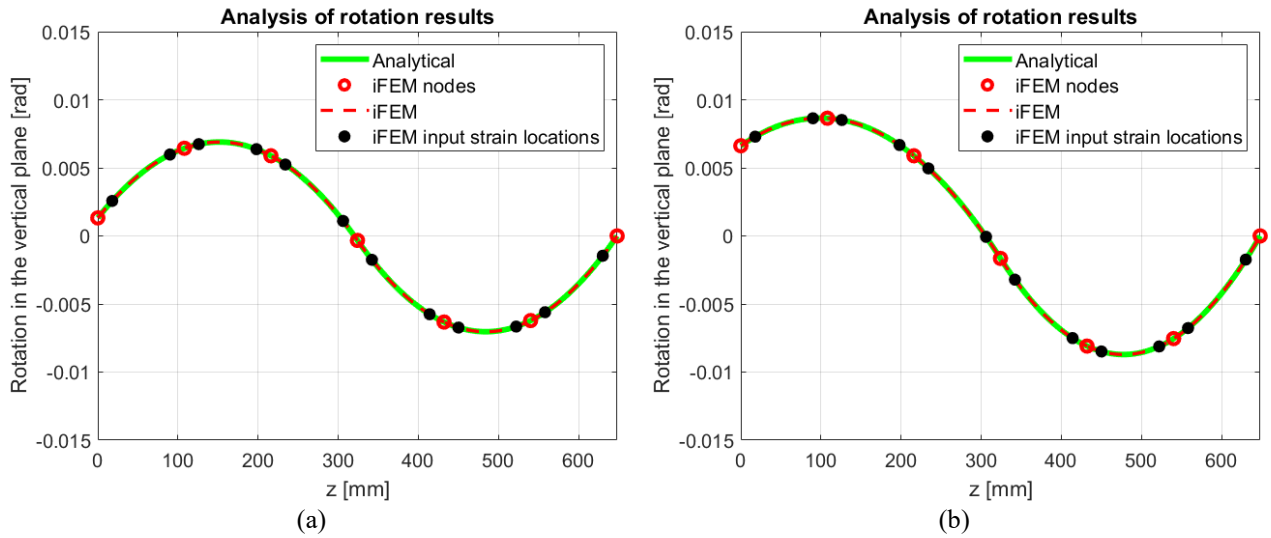

Figure 10 Reconstructed rotations for the beam with a degrading rotational boundary condition at the left end: (a) 10% degradation; (b) 50% degradation.

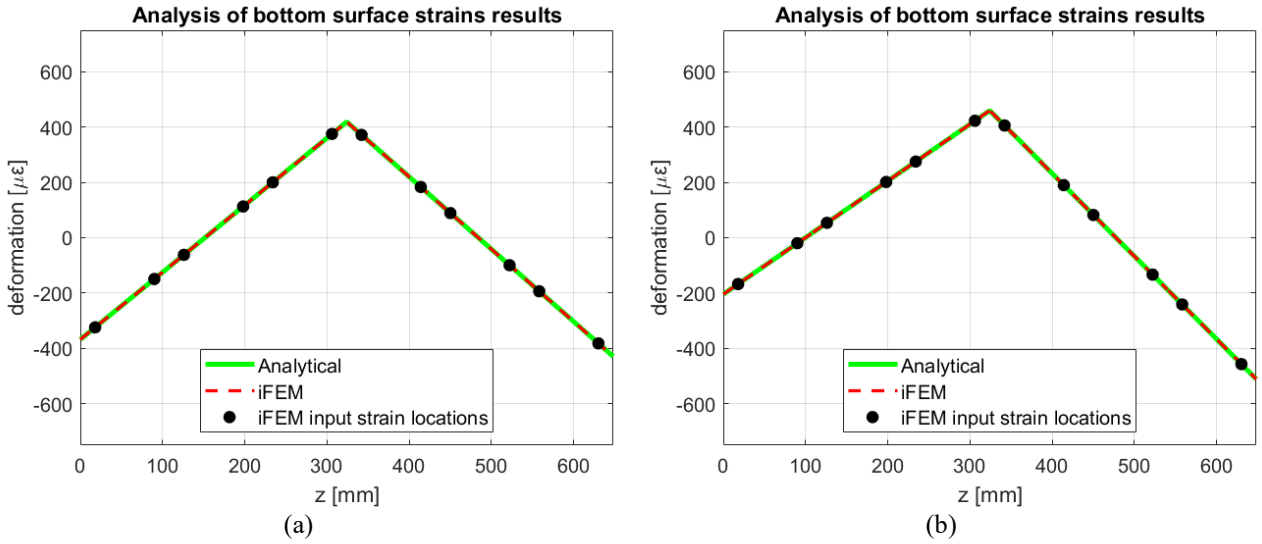

Figure 11 Reconstructed bottom strains for the beam with a degrading rotational boundary condition at the left end: (a) 10% degradation; (b) 50% degradation.

Specifically, a rotation of $0.0001324\ rad$ was applied, corresponding to a nominal degradation level of 1%, considered as reference (healthy) condition for the calculation of $\Delta k_{\varphi_{\%}}$. Selecting excessively small values of k_{TARGET_0} would result in similar $\Delta k_{\varphi_{\%}}$ values for higher degradation levels (e.g., 40% and 50%), reducing the resolution of the degradation metric. Additionally, imposing excessively small displacements or rotations can result in extremely large stiffness coefficients, which may lead to an ill-conditioned and potentially unstable stiffness matrix.

Table 2 Comparison between stiffness coefficients simulated by FEM analysis and equivalent stiffness coefficients obtained from the proposed method for different levels of rotational degradation.

Degradation level [%]	$k_{TARGET}\left[\frac{Nmm}{rad}\right]$	$k_{iFEM}\left[\frac{1}{rad}\cdot 10^{-8}\right]$
1	178,242,000	319.78
5	34,208,100	81.80
10	16,203,800	59.08
20	7,201,720	13.23
30	4,201,010	11.21
40	2,700,650	8.82
50	1,800,440	9.02

The expected decreasing trend of the stiffness coefficient with increasing rotation, and thus boundary degradation, is generally respected in the estimated k_{iFEM} values (Table 2). The only exception occurs at the 50% degradation level, where the estimated equivalent stiffness is slightly higher than that of the previous degradation level. This deviation may be attributed to the very small magnitude of the resulting stiffness values (on the order of 10^{-8}), which can introduce numerical inaccuracies in the optimization process due to finite precision and convergence tolerances. Nevertheless, the discrepancy is minimal: the difference in degradation percentage between the 40% and 50% levels ($\Delta k_{\varphi_{\%,iFEM}}$) is only 0.06%, as can be seen in Table 3.

Moreover, Table 3 shows that the absolute difference between the degradation percentages computed from FEM stiffness values ($\Delta k_{\varphi_{\%,TARGET}}$) and from iFEM estimated values ($\Delta k_{\varphi_{\%,iFEM}}$), denoted as

$|\Delta k_{\varphi_{\%,diff}}|$, is consistently below 10%. This supports the reliability of the proposed method in accurately reconstructing the degraded boundary stiffness in the case of rotational degradation.

Table 3 Comparison between the reference degree of degradation and the estimated degree of degradation obtained from iFEM at different levels of rotational degradation.

Degradation level [%]	$\mathbf{\Delta k_{\varphi_{\%,TARGET}}}$ [%]	$\mathbf{\Delta k_{\varphi_{\%,iFEM}}}$ [%]	$\mathbf{\lvert\Delta k_{\varphi_{\%,diff}}\rvert}$ [%]
1	0	0	0
5	-80.81	-74.42	6.39
10	-90.91	-81.52	9.39
20	-95.96	-95.86	0.10
30	-97.64	-96.49	1.15
40	-98.49	-97.24	1.25
50	-98.99	-97.18	1.81

Furthermore, Table 3 shows that $\Delta k_{\varphi_{\%,TARGET}}$ and $\Delta k_{\varphi_{\%,iFEM}}$ tend to follow an asymptotic trend as the degradation level increases. This behavior is consistent with the expected response of a virtual spring, whose stiffness is theoretically governed by a hyperbolic relationship with respect to the imposed displacement. As a result, the change in stiffness diminishes at higher displacement levels. This trend is visible in Figure 12, where the estimated equivalent stiffness coefficients have been fitted using two different models.

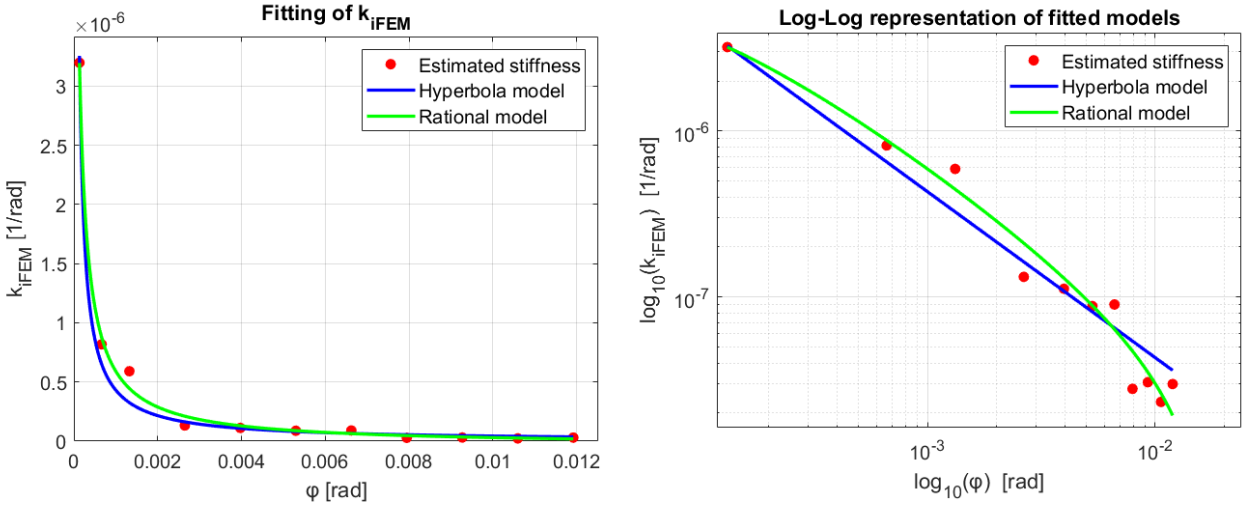

(a) (b)

Figure 12 Fitted behavior of the equivalent stiffness coefficient as a function of the rotation at the constraint: (a) fitted solutions in the real scale; (b) fitted solutions in log-log scale.

To clarify the stiffness–rotation trend at larger rotations, additional equivalent-stiffness points (60%, 70%, 80%, 90% degradation) were obtained from the optimization. The data were then fitted with two models: a hyperbola model and a rational model.

$$\begin{cases} k(\varphi) = \dfrac{f}{\varphi} \\ k(\varphi) = \dfrac{a + b \cdot \varphi}{c + d \cdot \varphi} \end{cases} \tag{29}$$

Where the parameters a, b, c, d, and f were optimized using a least-squares approach, minimizing the discrepancy between the fitted model and the data points of equivalent stiffness.
Although the hyperbolic function is physically more representative of the underlying mechanical behavior, Figure 12 reveals that the rational model provides a better fit, especially in the log-log plot. This observation is further supported by the performance metrics reported in Table 4, where a comparison of the two fitting models is presented, including:

- the Adjusted R-squared (Adj. R^2, $Adj.R^2 = 1 - \left(\frac{(1-R^2)(N-1)}{N-p-1}\right)$), where R^2 is the coefficient of determination, N the number of observations and p the number of predictors (independent features);
- Root Mean Square Error (RMSE, $\mathrm{RMSE} = \sqrt{\frac{1}{N} \cdot \sum_{i=1}^{N}(y_i - \hat{y}_i)^2}$);
- Mean Absolute Error (MAE, $\mathrm{MAE} = \frac{1}{N} \cdot \sum_{i=1}^{N}|y_i - \hat{y}_i|$);
- Symmetric Mean Absolute Percentage Error (SMAPE, $\mathrm{SMAPE} = \frac{100\%}{N} \cdot \sum_{i=1}^{N} \frac{|\hat{y}_i - y_i|}{(|y_i| + |\hat{y}_i|)/2}$).

Table 4 Performance metrics for the comparison of the two fitting models used for the estimation of k_{iFEM} behavior with respect to the rotation at the constraint.

Model type	Adj. R^2	RMSE $\left[\frac{1}{rad} \cdot 10^{-8}\right]$	MAE $\left[\frac{1}{rad} \cdot 10^{-8}\right]$	SMAPE [%]
Hyperbola	0.9870	9.74	5.65	29.49
Rational	0.9939	5.46	3.48	22.80

It is worth noting that both the hyperbolic and rational models belong to the same family of rational functions. This implies that, despite their different complexity levels, they share similar structural characteristics and can approximate each other under certain parameter combinations. Therefore, adopting a more flexible rational form does not contradict the physical interpretation provided by the hyperbolic model, but rather extends its descriptive power to better capture the nuances of the data, especially in the presence of numerical noise and non-ideal boundary behavior.
However, a known limitation of the rational model in this context is that it tends to a constant value $\frac{a}{c}$ as $\varphi \to 0$, whereas the physical stiffness is expected to diverge, ideally tending to infinity. This discrepancy makes the rational model less accurate in capturing the behavior of very stiff boundary conditions when extrapolating the fit beyond the range of degradation levels used for calibration. This limitation should be considered when interpreting the results, particularly in scenarios involving near-rigid boundary conditions.
It is important to note that the RMSE of the rational model fit exceeds the calculated k_{iFEM} value at the 60% degradation level, while the hyperbolic model's RMSE already exceeds the k_{iFEM} value at the 40% level. This suggests that beyond these thresholds, the stiffness coefficients estimated by the respective models become increasingly unreliable. Once again, this emphasizes the rational model's superior ability to fit the observed data across a wider degradation range. However, even a well-fitting model does not resolve the inherent limitation of k_{iFEM}: its lack of direct physical units. In practical applications, particularly when material properties and the exact original boundary stiffness are unknown, the outcomes presented in Figure 12 are not sufficient to accurately characterize structural health, as the units of k_{iFEM} lack direct physical meaning.
This limitation underscores the importance of having a reliable reference relation to convert the estimated k_{iFEM} values into physically meaningful stiffness coefficients, as explained in Section 3. Such a conversion is crucial for performing actionable structural assessments, including the design

of appropriate reinforcements to restore the original constraint condition. Figure 13 shows the relation between k_{iFEM} and k_{TARGET} for this scenario.
The data points, representing corresponding values of stiffness at each degradation level, were interpolated to observe an underlying trend. While this trend is not easily captured by a simple analytical expression, both a linear and a power-law fit were applied.
Table 5 presents the same performance metrics used earlier in Table 4 for comparison purposes. The results show that although the Adj. R^2 values are high, indicating good overall fit, the RMSE suggests a notable limitation: both models fail to accurately estimate the k_{TARGET} values associated with degradation levels above 50%, as the RMSE exceeds the actual k_{TARGET} at that threshold. Furthermore, the SMAPE values are considerably high, indicating that the model's average percentage error is close to the magnitude of the values themselves. It is also worth noting that the high-stiffness (low degradation) range remains relatively sparse. Therefore, acquiring additional data points in this regime would be necessary to improve the reliability and resolution of the fitted relationship.

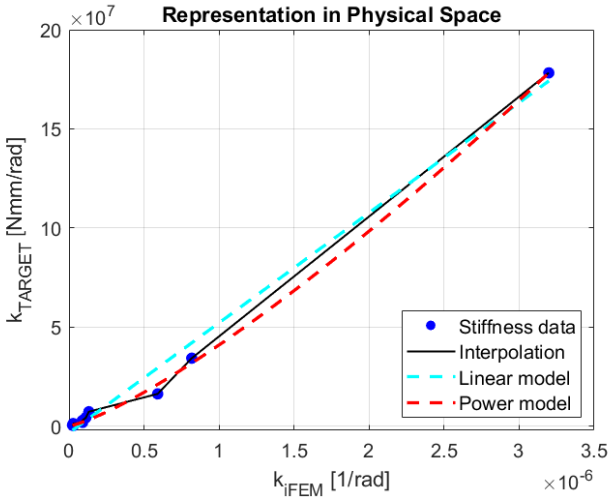

Figure 13 Relation between k_{iFEM} and k_{TARGET} for the rotational degradation class in real scale representation.

Table 5 Performance metrics for the comparison of the two fitting models used for the estimation of relation between k_{iFEM} and k_{TARGET} for the rotational degradation class.

Model type	Adj. R^2	RMSE $\left[\frac{1}{rad} \cdot 10^{-8}\right]$	MAE $\left[\frac{1}{rad} \cdot 10^{-8}\right]$	SMAPE [%]
Linear	0.9869	5.15	3.79	96.69
Power	0.9978	2.13	1.40	40.57

Finally, Table 6 and Table 7 present the results of the two alternative methods described in Sections 2.4.1 and 2.4.2, corresponding to Case A and Case B, respectively.
Table 6 reports the comparison between the reference stiffness values and the corresponding estimates obtained for Case A, including the computed percentage difference at each degradation level. Conversely, Table 7 reports the comparison between the estimated and reference degradation levels for Case B, along with the absolute differences observed at each level.
Both methods yield estimates closely aligned with the reference targets; Case B nearly matches the reference degradation across all instances. Nonetheless, both approaches rely on strong assumptions: Case A requires a known, time-invariant elastic modulus E; Case B does not require prior E but still

assumes E is constant. In practice, both boundary constraints and material properties may degrade, limiting the applicability of these methods unless such assumptions are verified

Table 6 Comparison between reference stiffness and estimated stiffness obtained from Case A at different levels of rotational degradation.

Degradation level [%]	$k_{TARGET}\left[\frac{Nmm}{rad}\right]$	$k_{estimated}\left[\frac{Nmm}{rad}\right]$	$Difference$ [%]
1	178,242,000	178,242,164	< 0.0001
5	34,208,100	34,208,115	< 0.0001
10	16,203,800	16,203,812	< 0.0001
20	7,201,720	7,201,720	0
30	4,201,010	4,201,000	< 0.0003
40	2,700,650	2,700,656	< 0.0003
50	1,800,440	1,800,438	< 0.0002

Table 7 Comparison between the reference degree of degradation and the estimated degree of degradation obtained from Case B at different levels of rotational degradation.

Degradation level [%]	$\Delta\mathbf{k}_{\boldsymbol{\varphi}\%,TARGET}$ [%]	$\Delta\mathbf{k}_{\boldsymbol{\varphi}\%,estimated}$ [%]	$\lvert\Delta\mathbf{k}_{\boldsymbol{\varphi}\%,diff}\rvert$ [%]
1	0	0	< 0.0001
5	-80.81	-80.81	< 0.0001
10	-90.91	-90.91	< 0.0001
20	-95.96	-95.96	< 0.0001
30	-97.64	-97.64	< 0.0001
40	-98.49	-98.49	< 0.0001
50	-98.99	-98.99	< 0.0001

5.3 Vertical settlement analysis

For the vertical settlement scenario, Figures 14, 15 and 16 show the reconstructed displacements, rotations, and bottom surface strains, respectively, for two representative degradation levels corresponding to 2% and 5% of the maximum allowed displacement ($28.60\ mm$), as detailed in Section 4.2.

The vertical displacement imposed at the degrading boundary condition is $0.57\ mm$ for degradation level equal to 2% and $1.48\ mm$ for degradation level equal to 5%. As shown in the figures, the two degradation levels are clearly distinguishable and the iFEM reconstruction closely follows the analytical deformed shape (and so the comparator measures). This confirms that, similarly to the rotational degradation scenario, the iFEM is effective in accurately reconstructing the structural response, yielding MPD values across different degradation levels always below 7%. Table 8 and Table 9 represent the results on the estimation of the equivalent stiffness coefficients. Similarly to Tables 2 and 3, they include the equivalent stiffness coefficients k_{iFEM}, the reference stiffness values of the TPU spacer plates $k_{TARGET} = k_{TPU}$ and the computed degree of degradation $\Delta k_{v\%}$.

Similarly to Section 5.2, to accurately evaluate $\Delta k_{v\%}$, the reference stiffness value for the healthy configuration (k_{TARGET_0}) was extracted from a FEM simulation, as explained in Section 3, imposing a vertical displacement of $0.286\ mm$, corresponding to a nominal degradation level of 1%. As expected, k_{iFEM} decreases as the degradation level increases, except for the 15% level. Like the 50% level of the rotational degradation scenario shown in Table 2, the estimated equivalent stiffness at 15% is slightly higher than that at 12%.

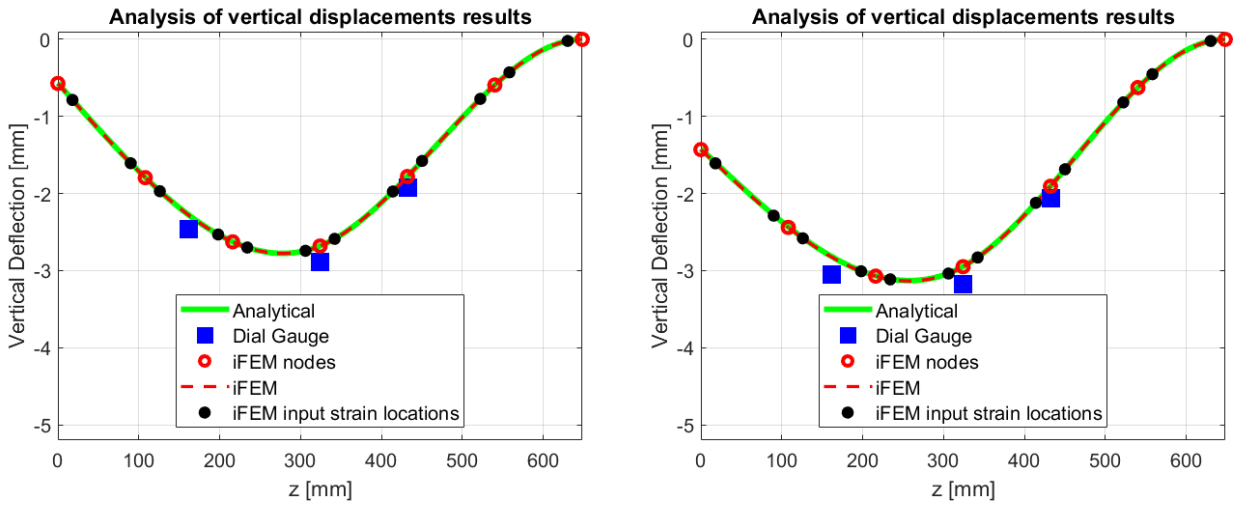

Figure 14 Reconstructed vertical displacements for the beam with a degrading vertical boundary condition at the left end: (a) 2% degradation; (b) 5% degradation.

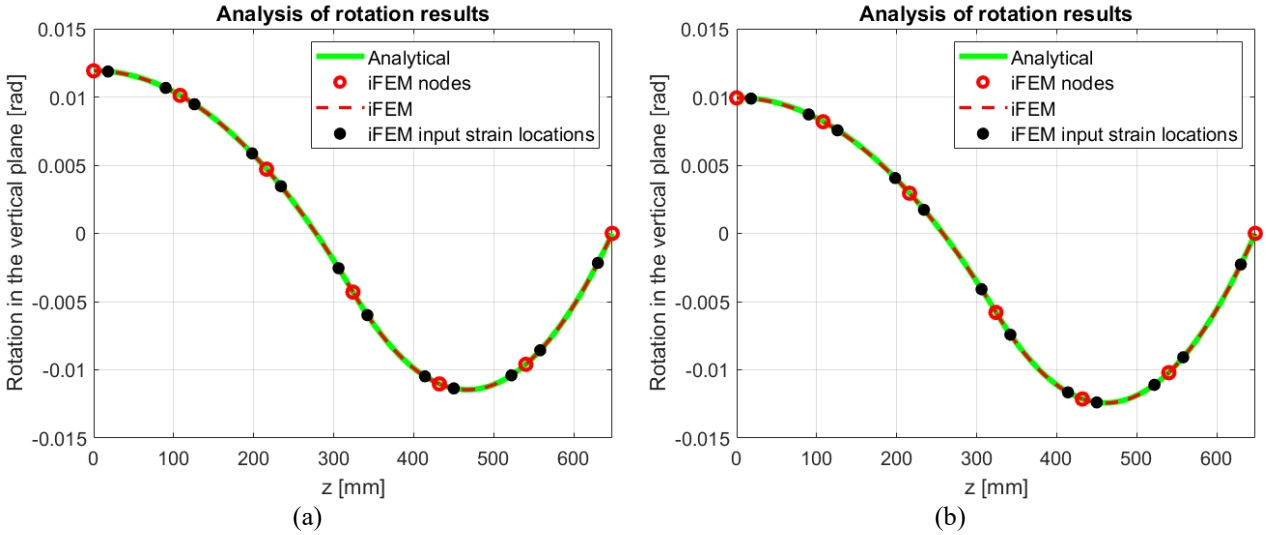

Figure 15 Reconstructed rotations for the beam with a degrading vertical boundary condition at the left end: (a) 2% degradation; (b) 5% degradation.

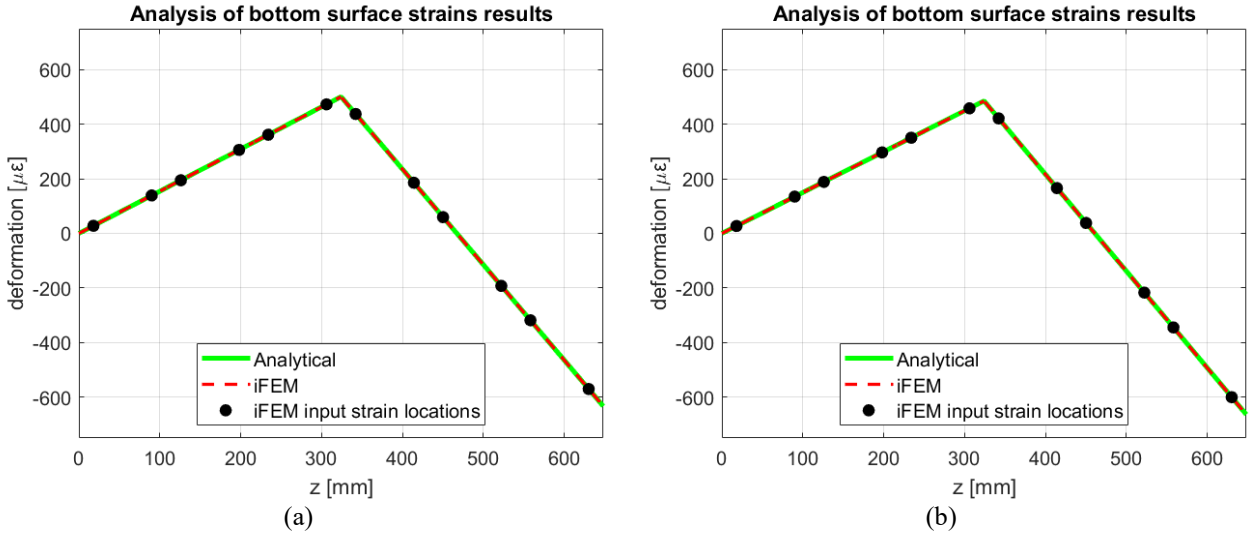

Figure 16 Reconstructed bottom strains for the beam with a degrading vertical boundary condition at the left end: (a) 2% degradation; (b) 5% degradation.

Table 8 Comparison between stiffness coefficients of TPU spacer plates and equivalent stiffness coefficients obtained from the proposed method for different levels of vertical displacement degradation.

Degradation level [%]	$k_{TARGET}\left[\frac{N}{mm}\right]$	$k_{iFEM}\left[\frac{1}{mm}\cdot 10^{-10}\right]$
1	320.74	646.66
1.5	212.76	250.48
2	158.76	162.25
5	61.58	54.33
10	29.18	13.01
12	23.78	9.62
15	18.38	17.24

Table 9 Comparison between the degree of degradation of TPU spacer plates' stiffness coefficients and equivalent stiffness coefficients at different levels of vertical displacement degradation.

Degradation level [%]	$\Delta k_{v\%,TARGET}$ [%]	$\Delta k_{v\%,iFEM}$ [%]	$\lvert\Delta k_{v\%,diff}\rvert$ [%]
1	0	0	0
1.5	-33.67	-61.27	7.60
2	-50.50	-74.91	4.41
5	-80.80	-91.60	10.80
10	-90.90	-97.99	7.09
12	-92.59	-98.51	5.92
15	-94.27	-97.33	3.06

This anomaly may be attributed to numerical errors, as the stiffness involved are extremely small (on the order of 10^{-10}), challenging the optimizer's numerical stability. This behavior tends to appear at higher degradation levels, which is reasonable as the boundary stiffness approaches zero.

It is also notable in Table 9 that the vertical degradation scenario exhibits a maximum $|\Delta k_{v\%,diff}|$ of nearly 10%, which is comparable with the one observed in the rotational scenario in Table 3. This suggests that the algorithm performs accurately in both rotational and vertical degradation. Furthermore, k_{iFEM} appears to decrease more rapidly than k_{TARGET}.

Additionally, Table 9 shows that both $\Delta k_{v\%,TARGET}$ and $\Delta k_{v\%,iFEM}$ exhibit an asymptotic trend as the degradation level increases. This behavior aligns with the theoretical response of a virtual spring, whose stiffness is expected to follow a hyperbolic relationship with respect to the imposed displacement, similarly to the rotational degradation scenario.

This trend can be observed in Figure 17, where the estimated equivalent stiffness coefficients have been fitted using the two models presented in Eq. (29), modified to consider vertical displacements at the boundary and with different parameters. To improve the understanding of the stiffness–displacement trend, particularly near the limit of validity of the small displacement theory, an additional equivalent stiffness point corresponding to 18% degradation was extracted from the optimization procedure. As shown in the log-log scale of Figure 17, the resulting k_{iFEM} value at this degradation level is significantly lower than the others, further emphasizing the approach to the highly non-linear behavior of the virtual spring. The fitting results indicate that the hyperbolic model, while physically representative of the underlying mechanical behavior, fails to accurately describe the response, as the displacements approach the limits of the small displacement theory.

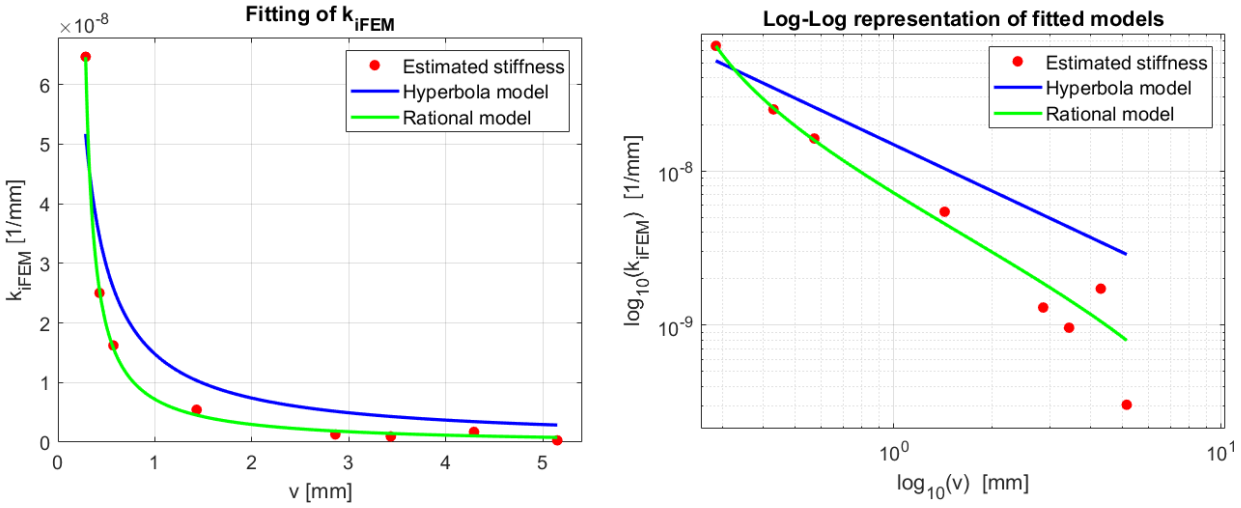

Figure 17 Fitted behavior of the equivalent stiffness coefficient as a function of the vertical displacement at the constraint: (a) fitted solutions in the real scale; (b) fitted solutions in log-log scale.

In contrast, the rational model significantly outperforms the hyperbolic function, offering greater flexibility due to its additional degrees of freedom and demonstrating improved adaptability to the data. The comparative performance of the two fitting models is summarized in Table 10, which reports key metrics consistent with the evaluation criteria used in Table 5.

Table 10 Performance metrics for the comparison of the two fitting models used for the estimation of k_{iFEM} behavior with respect to the displacement at the constraint.

Model type	Adj. R^2	RMSE $\left[\frac{1}{mm} \cdot 10^{-10}\right]$	MAE $\left[\frac{1}{mm} \cdot 10^{-10}\right]$	SMAPE [%]
Hyperbola	0.8610	41.53	30.55	49.62
Rational	0.9983	5.57	5.10	29.56

It is important to note that the RMSE of the rational model fit exceeds the calculated k_{iFEM} value at the 18% degradation level, while the hyperbolic model's RMSE already exceeds the k_{iFEM} value at the 5% level, suggesting that beyond these thresholds, the stiffness coefficients estimated by the respective models become increasingly unreliable. Once again, even in the vertical settlement scenario, it is emphasized how the rational model is superior in fitting the observed data.

However, the results presented in Figure 17 are not sufficient to perform structural assessment and provide proper strategies of reinforcement design for the degraded constraint. Therefore, the relation between k_{iFEM} and k_{TARGET} should be developed, as the one discussed in Section 5.2 for the rotational degradation scenario.

Without loss of generality, Figure 18 shows this relation presented on a real scale. The data points represent corresponding values of stiffness at each degradation level and were interpolated to observe the underlying trend. A linear and a power-law fit were applied, because this trend was not easily captured by a simple analytical expression.

Table 11 presents the same performance metrics used earlier in Tables 4, 5 and 10 for comparison purposes. Like the rotational degradation scenario, the results indicate that although the Adj. R^2 values are relatively high, suggesting a good overall fit, the RMSE reveals important limitations. Specifically, the linear model fails to accurately estimate the k_{TARGET} values above the 5%

degradation level, as its RMSE exceeds the actual k_{TARGET} at that threshold. The power-law model performs better, although its RMSE remains comparable to the k_{TARGET} value corresponding to the 18% degradation level, indicating a reduced reliability in the higher degradation levels. In this analysis, the SMAPE values appear relatively small, suggesting theoretically good predictive accuracy; however, this result is likely biased by the limited number of available data points, which undermines the robustness of the metric. For this scenario, the entire range of degradation is sparsely populated, consequently, additional data across the full degradation spectrum should be collected to improve the reliability, stability, and interpretability of fitted relationships.

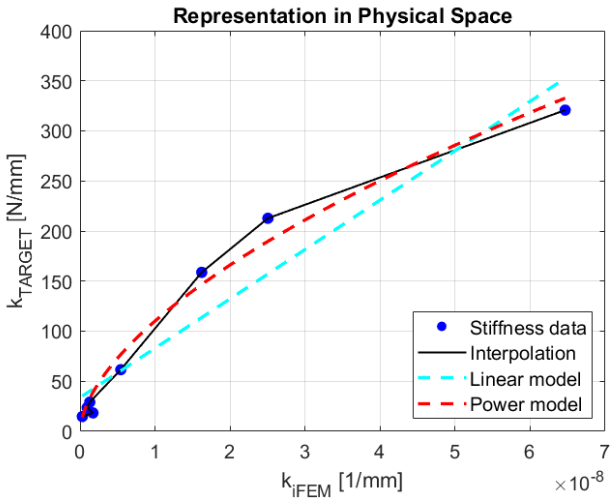

Figure 18 Relation between k_{iFEM} and k_{TARGET} for the vertical settlement scenario.

Table 11 Performance metrics for the comparison of the two fitting models used for the estimation of relation between k_{iFEM} and k_{TARGET} for the vertical settlement scenario.

Model type	Adj. R^2	RMSE $\left[\frac{N}{mm}\right]$	MAE $\left[\frac{N}{mm}\right]$	SMAPE [%]
Linear	0.8853	30.51	25.42	39.20
Power	0.9769	13.69	11.38	18.62

In parallel with the analysis of the rotational degradation scenario, Table 12 and Table 13 present the results of the alternative method described in Section 2.4.4. This approach follows the same principles as those adopted in Case A and Case B (Sections 2.4.1 and 2.4.2), adapted to evaluate boundary stiffness and degree of degradation based on shear force observations. Specifically, Table 12 compares the reference stiffness values with the corresponding estimates obtained for Case A, including the computed percentage differences at each degradation level. Table 13 complements this analysis by reporting the estimated degradation levels for Case B alongside the reference values and the absolute differences observed. Consistent with the results from the rotational scenario (Table 6 and Table 7), the estimates obtained here show strong agreement with the reference targets, particularly in the estimation of the degree of degradation.

However, these results rely on the same key assumption discussed in Sections 2.4.1 and 2.4.2, that the material property E remains constant across all degradation levels. In practice, this may not hold, as material properties often degrade alongside boundary conditions. Therefore, the applicability of these methods should be considered with caution.

Table 12 Comparison between reference stiffness and estimated stiffness obtained from Case A at different levels of vertical settlement.

Degradation level [%]	$k_{TARGET}\left[\frac{N}{mm}\right]$	$k_{estimated}\left[\frac{N}{mm}\right]$	$Difference$ [%]
1	320.74	318.38	0.74
5	212.76	211.19	0.74
10	158.76	157.59	0.74
20	61.58	61.12	0.75
30	29.18	28.97	0.72
40	23.78	23.61	0.72
50	18.38	18.25	0.71

Table 13 Comparison between the reference degree of degradation and the estimated degree of degradation obtained from Case B at different levels of vertical settlement.

Degradation level [%]	$\Delta k_{\%,TARGET}$ [%]	$\Delta k_{\%,estimated}$ [%]	$\lvert\Delta k_{\%,diff}\rvert$ [%]
1	0	0	< 0.0001
1.5	-33.67	-33.67	< 0.0001
2	-50.50	-50.50	< 0.0001
5	-80.80	-80.80	< 0.0001
10	-90.90	-90.90	< 0.0001
12	-92.59	-92.59	< 0.0001
15	-94.27	-94.27	< 0.0001

6. Concluding Remarks

This study addressed the problem of monitoring the progressive degradation of boundary conditions in beam-like structures, a phenomenon that can significantly affect global structural behavior over time. Motivated by real-world scenarios in which boundary conditions deteriorate due to damage, aging, or improper installation, the proposed methodology combines strain measurements with the inverse Finite Element Method (iFEM) to enable continuous and distributed structural assessment.

The work extends the application of iFEM to structures with non-ideal boundary conditions, where the standard formulation becomes incompatible with the actual physical system, resulting in inaccurate displacement and strain field reconstructions. To address this issue, a comprehensive framework is introduced to model and analyze structures affected by support degradation—an essential step for the effective deployment of Structural Health Monitoring (SHM) systems aimed at improving safety and reducing maintenance costs. A central innovation of the proposed framework lies in a novel approach for estimating boundary stiffness from strain measurements, allowing the numerical model to dynamically adapt to evolving boundary conditions. The methodology is demonstrated across three application cases, each reflecting a different level of prior knowledge regarding material properties and initial boundary configurations.

The main features and findings of the proposed methodology can be summarized as follows:

- *General applicability*: In the most challenging scenario—where neither the material properties nor the initial boundary stiffness is known—a novel identification strategy is proposed to estimate the equivalent boundary stiffness.
- *Framework flexibility*: The proposed approach is fully general and can accommodate multiple degrading degrees of freedom by acting simultaneously, making it suitable for a wide range of practical applications.
- *Shape sensing with experimental validation*: The framework was experimentally validated on an aluminum beam subjected to two types of boundary degradation:
  - Rotational degradation: iFEM-based shape sensing showed excellent performance, with a mean percentage difference (MPD) below 1%.
  - Vertical settlement: Shape sensing accuracy remained satisfactory, with an MPD below 7%.
- *Degradation estimation accuracy*:
  - In the rotational degradation scenario, the estimated stiffness degradation deviated by less than 10% from the reference values across all tested levels.
  - In the vertical settlement scenario, estimation errors were approximately the same as the rotational case, with a maximum deviation of approximately 10%.
- *Physical consistency*: The estimated stiffness values exhibited physically consistent trends as degradation increased, reinforcing the reliability of the approach. However, some discrepancies in the degradation estimation were observed.
- *Current limitations*: A key limitation of the study is the lack of a clear correlation between the estimated equivalent stiffness by iFEM and physically interpretable stiffness parameters, mainly due to the limited experimental dataset. Also, the method is applicable to hyperstatic structures only.

This framework addresses a current gap in the literature by linking boundary condition characterization—traditionally tackled through vibration-based or modal analyses—with strain-based

inverse finite element modeling. By integrating accurate boundary modeling into shape sensing, the methodology enhances the potential of SHM strategies to capture evolving structural conditions over time, including support degradation and maintenance interventions. Future research will aim to improve the robustness of the stiffness identification process, incorporate data-driven prognostic models for life-cycle prediction, and extend the framework to more complex and combined degradation scenarios.

CRediT author statement

Jacopo Bardiani: Conceptualization, Methodology, Validation, Formal Analysis, Investigation, Data curation, Writing—original draft preparation, Writing—review and editing, Visualization. **Francesco Orsenigo:** Conceptualization, Methodology, Validation, Formal Analysis, Investigation, Data curation, Writing—original draft preparation, Writing—review and editing, Visualization. **Andrea Manes:** Resources, Methodology, Writing—review and editing, Supervision, Project administration. **Claudio Sbarufatti:** Conceptualization, Methodology, Resources, Writing—review and editing, Supervision, Project administration.

All authors have read and agreed to the published version of the manuscript.

Declaration of competing interest

The author(s) declared no potential conflicts of interest with respect to the research, authorship, and/or publication of this article.

ORCID iD

Jacopo Bardiani https://orcid.org/0000-0003-4572-8073

Andrea Manes https://orcid.org/0000-0001-7485-8980

Claudio Sbarufatti https://orcid.org/0000-0001-5511-8194

Data Availability Statement

The data given in this article are the data supporting the results of this study are available upon request.

References

1. Zhang G, Liu Y, Liu J, et al. Causes and statistical characteristics of bridge failures: a review. J Traffic Transp Eng (Engl Ed) 2022; 9(3): 388–406. DOI: 10.1016/j.jtte.2021.12.003.
2. Biezma MV, Schanack F. Collapse of steel bridges. J Perform Constr Facil 2007; 21(5): 398–405. DOI: 10.1061/(ASCE)0887-3828(2007)21:5(398).
3. Penttala V. Causes and mechanisms of deterioration in reinforced concrete. In: Delatte N, *Failure, distress and repair of concrete structures*. 1st ed. Cambridge: Woodhead Publishing, 2009, pp.3–31. DOI: 10.1533/9781845697037.1.3.
4. Deng L, Wang W, Yu Y. State-of-the-art review on the causes and mechanisms of bridge collapse. J Perform Constr Facil 2016; 30(2): 04015005.
5. Choudhury JR, Hasnat A. Bridge collapses around the world: causes and mechanisms. In: *IABSE-JSCE Joint Conference on Advances in Bridge Engineering-III*. Dhaka, Bangladesh, 21–22 August 2015.
6. AASHTO. *LRFD bridge design specifications*. 8th ed. Washington, DC: American Association of State Highway and Transportation Officials, 2017. ISBN: 978-1-56051-654-5.
7. Poonguzhali A, Shaikh H, Dayal RK, et al. A review on degradation mechanism and life estimation of civil structures. Corros Rev 2008; 26(4): 215–294. DOI: 10.1515/corrrev.2008.215.
8. Talebinejad I, Fischer C, Ansari F. Numerical evaluation of vibration-based methods for damage assessment of cable-stayed bridges. Comput Aided Civ Infrastruct Eng 2011; 26(3): 239–251. DOI: 10.1111/j.1467-8667.2010.00684.x.
9. Oskoui EA, Taylor TB, Ansari F. Method and monitoring approach for distributed detection of damage in multi-span continuous bridges. Eng Struct 2019; 189: 385–395. DOI: 10.1016/j.engstruct.2019.02.037.
10. Nazarian E, Ansari F, Zhang XT, et al. Detection of tension loss in cables of cable-stayed bridges by distributed monitoring of bridge deck strains. J Struct Eng 2016; 142(6): 04016018.
11. Gatti F. Ponte Morandi, le foto shock prima del crollo: travi rotte e cavi ridotti del 75 per cento. L'Espresso, https://lespresso.it/c/-/2018/9/13/ponte-morandi-le-foto-shock-prima-del-crollo-travi-rotte-e-cavi-ridotti-del-75-per-cento/10861 (2018, accessed 4 May 2025).
12. Commissione Ispettiva Ministeriale. Autostrada A10—Crollo del Viadotto Polcevera, evento accaduto il 14 Agosto 2018. Report for Ministero delle Infrastrutture e dei Trasporti, 25 September 2018, Rome, Italy, https://www.mit.gov.it/comunicazione/news/ponte-morandi-online-la-relazione-della-commissione-ispettiva-mit (accessed 4 May 2025).
13. Morgese M, Ansari F, Domaneschi M, et al. Post-collapse analysis of Morandi's Polcevera viaduct in Genoa, Italy. J Civ Struct Health Monit 2020; 10(1): 69–85. DOI: 10.1007/s13349-019-00370-7.
14. Chen H, Spyrakos CC, Venkatesh G. Evaluating structural deterioration by dynamic response. J Struct Eng 1995; 121(8): 1197–1204. DOI: 10.1061/(ASCE)0733-9445(1995)121:8(1197).
15. Farrar CR, Worden K. An introduction to structural health monitoring. Philos Trans A Math Phys Eng Sci 2007; 365: 303–315. DOI: 10.1098/rsta.2006.1928.
16. Helmi K, Taylor T, Zarafshan A, et al. Reference free method for real time monitoring of bridge deflections. Eng Struct 2015; 103: 116–124. DOI: 10.1016/j.engstruct.2015.09.002.
17. Wang C, Ansari F, Wu B, et al. LSTM approach for condition assessment of suspension bridges based on time-series deflection and temperature data. Adv Struct Eng 2022; 25(16): 3450–3463. DOI: 10.1177/13694332221133604.

18. Abdulkarem M, Samsudin K, Rokhani FZ, et al. Wireless sensor network for structural health monitoring: a contemporary review of technologies, challenges, and future direction. Struct Health Monit 2020; 19: 693–735. DOI: 10.1177/1475921719854528.
19. Güemes A, Fernández-López A, Díaz-Maroto PF, et al. Structural health monitoring in composite structures by fiber-optic sensors. Sensors 2018; 18: 1094. DOI: 10.3390/s18041094.
20. Seguel F, Meruane V. Damage assessment in a sandwich panel based on full-field vibration measurements. J Sound Vib 2018; 417: 1–18. DOI: 10.1016/j.jsv.2017.11.048.
21. Gulizzi V, Rizzo P, Milazzo A, et al. An integrated structural health monitoring system based on electromechanical impedance and guided ultrasonic waves. J Civ Struct Health Monit 2015; 5: 337–352. DOI: 10.1007/s13349-015-0112-0.
22. Bhuiyan MY, Bao J, Poddar B, et al. Toward identifying crack-length-related resonances in acoustic emission waveforms for structural health monitoring applications. Struct Health Monit 2018; 17: 577–585. DOI: 10.1177/1475921717707356.
23. Kral Z, Horn W, Steck J. Crack propagation analysis using acoustic emission sensors for structural health monitoring systems. Sci World J 2013; 2013: 823603. DOI: 10.1155/2013/823603.
24. Yang Y, Zhang Y, Tan X. Review on vibration-based structural health monitoring techniques and technical codes. Symmetry 2021; 13: 1998. DOI: 10.3390/sym13111998.
25. Ai D, Luo H, Zhu H. Diagnosis and validation of damaged piezoelectric sensor in electromechanical impedance technique. J Intell Mater Syst Struct 2017; 28: 837–850. DOI: 10.1177/1045389X16657427.
26. Xu Y, Brownjohn JMW, Huseynov F. Accurate deformation monitoring on bridge structures using a cost-effective sensing system combined with a camera and accelerometers: case study. J Bridge Eng 2019; 24: 05018014. DOI: 10.1061/(ASCE)BE.1943-5592.0001330.
27. Jin Z, Xia H, Ni W, et al. Reference point-free measurement of bridge dynamic deflection by fusing hydraulic leveling and accelerometer signals. Struct Control Health Monit 2023; 2023: 1–19. DOI: 10.1155/2023/3203261.
28. Moreu F, Li J, Jo H, et al. Reference-free displacements for condition assessment of timber railroad bridges. J Bridge Eng 2016; 21: 04015052. DOI: 10.1061/(ASCE)BE.1943-5592.0000805.
29. Xue MS, Yi TH, Qu CX, et al. Bridge flexibility identification through a reference-free substructuring integration method driven by mode fitting. J Eng Mech 2022; 148: 04021164. DOI: 10.1061/(ASCE)EM.1943-7889.0002082.
30. Sarwar MZ, Park JW. Bridge displacement estimation using a co-located acceleration and strain. Sensors 2020; 20: 1109. DOI: 10.3390/s20041109.
31. Ozdagli AI, Liu B, Moreu F. Measuring total transverse reference-free displacements for condition assessment of timber railroad bridges: experimental validation. J Struct Eng 2018; 144: 04018047. DOI: 10.1061/(ASCE)ST.1943-541X.0002041.
32. Aguero M, Ozdagli A, Moreu F. Measuring reference-free total displacements of piles and columns using low-cost, battery-powered, efficient wireless intelligent sensors (LEWIS2). Sensors 2019; 19: 1549. DOI: 10.3390/s19071549.
33. Moreu F, Chen L, Zhu C, et al. Measuring total transverse reference-free displacements of railroad bridges using two degrees of freedom: experimental validation. J Infrastruct Syst 2023; 29: 04023009. DOI: 10.1061/JITSE4.ISENG-2132.
34. Skafte A, Aenlle ML, Brincker R. A general procedure for estimating dynamic displacements using strain measurements and operational modal analysis. Smart Mater Struct 2016; 25: 025020. DOI: 10.1088/0964-1726/25/2/025020.

35. You RZ, Yi TH, Ren L, et al. Equivalent estimation method (EEM) for quasi-distributed bridge-deflection measurement using only strain data. Meas 2023; 221: 113492. DOI: 10.1016/j.measurement.2023.113492.
36. Stiros SC. GNSS (GPS) monitoring of dynamic deflections of bridges: structural constraints and metrological limitations. Infrastructures 2021; 6: 23. DOI: 10.3390/infrastructures6020023.
37. Foss G, Haugse E. Using modal test results to develop strain to displacement transformations. In: *Proceedings of the Thirteenth International Modal Analysis Conference*, Nashville, TN, USA, 13–16 February 1995, pp.112. Bethel, CT: SEM.
38. Pisoni AC, Santolini C, Hauf DE, et al. Displacements in a vibrating body by strain gage measurements. In: *Proceedings of SPIE – The International Society for Optical Engineering*, San Diego, CA, USA, 1–5 March 2001, pp.119–119. Bellingham, WA: SPIE.
39. Bogert P, Haugse E, Gehrki R. Structural shape identification from experimental strains using a modal transformation technique. In: *Proceedings of the 44th AIAA/ASME/ASCE/AHS/ASC Structures, Structural Dynamics, and Materials Conference*, Norfolk, VA, USA, 7–10 April 2003, paper no. AIAA-2003-1626. Reston, VA: AIAA.
40. Kang LH, Kim DK, Han JH. Estimation of dynamic structural displacements using fiber Bragg grating strain sensors. J Sound Vib 2007; 305: 534–542. DOI: 10.1016/j.jsv.2007.04.037.
41. Zhang P, Qing H. The consistency of the nonlocal strain gradient integral model in size-dependent bending analysis of beam structures. Int J Mech Sci 2021; 189: 105991. DOI: 10.1016/j.ijmecsci.2020.105991.
42. Hong W, Qin Z, Lv K, et al. An indirect method for monitoring dynamic deflection of beam-like structures based on strain responses. Appl Sci 2018; 8: 811. DOI: 10.3390/app8050811.
43. Tessler A, Spangler J. A variational principle for reconstruction of elastic deformations in shear deformable plates and shells. Report, NASA Langley Research Center Hampton, VA, United States. Report no. NASA/TM-2003-212445, August 2003.
44. Gherlone M, Cerracchio P, Mattone M. Shape sensing methods: review and experimental comparison on a wing-shaped plate. Prog Aerosp Sci 2018; 99: 14–26. DOI: 10.1016/j.paerosci.2018.04.001.
45. Tessler A, Spangler J. Inverse FEM for full-field reconstruction of elastic deformations in shear deformable plates and shells. In: *2nd European Workshop on Structural Health Monitoring*, Munich, Germany, 7-9 July 2004, Hampton, VA, USA: NASA Langley Research Center.
46. Gherlone M, Cerracchio P, Mattone M, et al. An inverse finite element method for beam shape sensing: theoretical framework and experimental validation. Smart Mater Struct 2014; 23(4): 045027. DOI: 10.1088/0964-1726/23/4/045027.
47. Gherlone M, Cerracchio P, Mattone M, et al. Beam shape sensing using inverse finite element method: theory and experimental validation. Struct Health Monit 2011; 1: 578–585.
48. Savino P, Gherlone M, Tondolo F. Shape sensing with inverse finite element method for slender structures. Struct Eng Mech 2019; 72: 217–227. DOI: 10.12989/SEM.2019.72.2.217.
49. Savino P, Tondolo F, Gherlone M, et al. Application of inverse finite element method to shape sensing of curved beams. Sensors 2020; 20(24): 7012. DOI: 10.3390/s20247012.
50. Quach CC, Vazquez SL, Tessler A, et al. Structural anomaly detection using fiber optic sensors and inverse finite element method. In: *Proceedings of the AIAA Guidance, Navigation, and Control Conference and Exhibit*, San Francisco, CA, USA, 15–18 August 2005, paper no. AIAA-2005-6357. Reston, VA: AIAA. DOI: 10.2514/6.2005-6357.
51. Poloni D, Oboe D, Sbarufatti C, et al. Debonding quantification in adhesive bonded joints by the inverse finite element method. Smart Mater Struct 2023; 32: 044002. DOI: 10.1088/1361-665X/acc0ee.

52. Oboe D, Colombo L, Sbarufatti C, et al. Comparison of strain pre-extrapolation techniques for shape and strain sensing by iFEM of a composite plate subjected to compression buckling. Compos Struct 2021; 262: 113587. DOI: 10.1016/j.compstruct.2021.113587.
53. Oboe D, Poloni D, Sbarufatti C, et al. Crack size estimation with an inverse finite element model. In: *Proceedings of the 10th European Workshop on Structural Health Monitoring (EWSHM 2022)*, edited by Rizzo P, Milazzo A; Palermo, Italy, 4–7 July 2022; Lecture Notes in Civil Engineering, vol 253, pp 443–453. Cham: Springer International Publishing. DOI: 10.1007/978-3-031-07254-3_45.
54. Poloni D, Oboe D, Sbarufatti C, et al. Towards a stochastic inverse finite element method: a Gaussian process strain extrapolation. Mech Syst Signal Process 2023; 164: 110056. DOI: 10.1016/j.ymssp.2022.110056.
55. Savino P, Tondolo F. A new approach for displacement and stress monitoring of tunnel based on iFEM methodology. Smart Mater Struct 2022; 31: 015013. DOI: 10.1088/1361-665X/ac3901.
56. Poloni D, Morgese M, Wang C, et al. Reference-free distributed monitoring of deflections in multi-span bridges. Eng Struct 2025; 323: 119277. DOI: 10.1016/j.engstruct.2024.119277.
57. Zhang Z, Zheng S, Li H, et al. Deflection estimation of truss structures using inverse finite element method. Sensors 2023; 23: 1716. DOI: 10.3390/s23031716.
58. Boukellif R, Ricoeur A. Identification of crack parameters and stress intensity factors in finite and semi-infinite plates solving inverse problems of linear elasticity. Acta Mech 2020; 231: 795–813. DOI: 10.1007/s00707-019-02575-9.
59. Boukellif R, Ricoeur A, Oxe M. Parameter identification of crack-like notches in aluminum plates based on strain gauge data. Struct Health Monit 2021; 20: 3227–3238. DOI: 10.1177/1475921720981845.
60. Waisman H, Chatzi E, Smyth AW. Detection and quantification of flaws in structures by the extended finite element method and genetic algorithms. Int J Numer Methods Eng 2010; 82: 303–328. DOI: 10.1002/nme.2766.
61. Rabinovich D, Givoli D, Vigdergauz S. Crack identification by 'arrival time' using XFEM and a genetic algorithm. Int J Numer Methods Eng 2009; 77: 337–359. DOI: 10.1002/nme.2416.
62. Liang YC, Sun YP. Hardware-in-the-loop simulations of hole/crack identification in a composite plate. Mater 2020; 13: 424. DOI: 10.3390/ma13020424.
63. Chen Y, Liu ZQ, Liu HL. Parameters identification for crack in elastic structures based on fiber Bragg grating. Optik 2018; 154: 685–691. DOI: 10.1016/j.ijleo.2017.10.126.
64. Nedelcu M. Optimisation of inverse finite element method for shape sensing of thin-walled cylinders by using generalised beam theory. Thin-Walled Structures 2023; 188: 110865. DOI: 10.1016/j.tws.2023.110865.
65. Craiu ID, Nedelcu M. Combining iFEM and GBT for accurate shape sensing and damage detection in truncated conical shells with circular cross-section. Ocean Engineering 2024; 311: 118811. DOI: 10.1016/j.oceaneng.2024.118811.
66. Zampieri P, Zanini MA, Faleschini F, et al. Failure analysis of masonry arch bridges subject to local pier scour. Eng Fail Anal 2017; 79: 371–384. DOI: 10.1016/j.engfailanal.2017.05.028.
67. Pezeshki H, Adeli H, Pavlou D, et al. State of the art in structural health monitoring of offshore and marine structures. Proc Inst Civ Eng Marit Eng 2023; 176(2): 89–108. DOI: 10.1680/jmaen.2022.027.
68. He M, Bai X, Ma R, et al. Structural monitoring of an onshore wind turbine foundation using strain sensors. Struct Infrastruct Eng 2019; 15(3): 314–333. DOI: 10.1080/15732479.2018.1546325.
69. Naresh M, Kumar V, Pal J, et al. A comprehensive review on health monitoring of joints in steel structures. Smart Mater Struct 2024; 33(7): 073004. DOI: 10.1088/1361-665X/ad5504.

70. Hasni H, Jiao P, Alavi AH, et al. Structural health monitoring of steel frames using a network of self-powered strain and acceleration sensors: a numerical study. Autom Constr 2018; 85: 344–357. DOI: 10.1016/j.autcon.2017.10.022.
71. Ahmadian H. Boundary condition identification by solving characteristic equations. J Sound Vib 2001; 247(5): 755–763. DOI: 10.1006/jsvi.2001.3708.
72. Liu W, Yang Z, Wang L, et al. Boundary condition modelling and identification for cantilever-like structures using natural frequencies. Chin J Aeronaut 2019; 32(6): 1451–1464. DOI: 10.1016/j.cja.2019.04.003.
73. Pabst U, Hagedorn P. Identification of boundary conditions as a part of model correction. J Sound Vib 1995; 182(4): 565–575. DOI: 10.1006/jsvi.1995.0217.
74. Qiao G, Rahmatalla S. Dynamics of Euler–Bernoulli beams with unknown viscoelastic boundary conditions under a moving load. J Sound Vib 2020; 479: 115771. DOI: 10.1016/j.jsv.2020.115771.
75. Nguyen XB, Pham TH, Nguyen DD. Using penalty method in identification of elastic fixed stiffness of frame structure. In: *Proceedings of the 3rd International Conference on Green Technology and Sustainable Development*, Da Nang, Vietnam, 25–26 November 2022. Les Ulis, France: EDP Sciences. DOI: 10.1051/e3sconf/202341003015.
76. Wang L, Guo N, Yang Z. Boundary condition identification of tapered beam with flexible supports using static flexibility measurements. Mech Syst Signal Process 2016; 70–71: 981–995. DOI: 10.1016/j.ymssp.2015.12.036.
77. Colombo L, Oboe D. Shape sensing and damage identification with iFEM on a composite structure subjected to impact damage and nontrivial boundary conditions. Mech Syst Signal Process 2020; 144: 107163. DOI: 10.1016/j.ymssp.2020.107163.
78. Ellobody E, Ran F, Young B. Review of the general steps of finite element analysis. In: Ellobody E, Ran F, Young B *Finite element analysis and design of metal structures*. 1st ed. Amsterdam, Netherlands: Elsevier, 2014, pp.15–30. DOI: 10.1016/B978-0-12-416561-8.00002-0.
79. MathWorks. Least-squares model fitting algorithms. MathWorks Help Center, https://it.mathworks.com/help/optim/ug/least-squares-model-fitting-algorithms.html (n.d., accessed 28 May 2025).
80. Byrd RH, Schnabel RB, Shultz GA. Approximate solution of the trust region problem by minimization over two-dimensional subspaces. Math Program 1988; 40: 247–263. DOI: 10.1007/BF01580735
81. FBGS. Draw tower gratings (DTGs). FBGS Technologies GmbH, https://fbgs.com/components/draw-tower-gratings-dtgs/ (2019, accessed 16 June 2025).